Solid State CQED
Quantum dots in microcavities

Bachelor Thesis

Evert van Nieuwenburg
Leiden University

Supervisors:
Cristian Bonato
Jan Gudat
Prof. Dirk Bouwmeester

July 14, 2010

Abstract

This thesis describes the properties of microcavities and quantum dots in a CQED experiment. Different (measurement) techniques (most notably the voltage scans, spatial scans and hole burning) are described, and are then used to demonstrate a procedure for making the fundamental cavity mode polarization degenerate. Polarization degeneracy is required for both practical reasons and for the eventual use in quantum computation algorithms. Multiple other measurements such as voltage-induced birefringence, reflection peak nonlinearity and strain induced quantum dot spectral shifting are discussed, as well as the characterization and calculations for the positioning sample. In the end, the aim of the experiment is to implement solid state storage qubits through electron spins, whilst data transfer and manipulation are done on photons that are spin-photon entangled (through the photon's polarization) with the qubits.

Contents

Chapter 1

Introduction

The quantum information and quantum computation fields have been making rapid advancements over the past few decades. One of the milestones yet to be reached is the implementation of a quantum computer. Theoretically, the quantum computer is able to achieve an exponential speed-up in the time required to perform some computationally expensive algorithms. An example is the factorization of prime numbers, which forms the basis of many important encryption algorithms today. Having a quantum computer to find the factorized prime numbers would render these encryptions useless. Somewhat ironically, a related field called **quantum cryptography** has provided a 100% secure way of data transfer [17]. These methods have been implemented, and are even commercially available. Apart from providing a very powerful computational speed-up, the quantum computer is the natural extension to the computers that exist nowadays (refered to simply as 'classical' computers). Since all the chips and circuits are getting smaller (and cheaper), there will be a point at which the quantum regime is reached. This regime might seem to be a hurdle to classical computers, but is essential for the extraordinary features of a quantum computer, the two most important features being **superposition** and **entanglement**.

Quantum computation as will be described in this thesis is in a sense a blend between quantum optics and quantum information. Quantum optics is the branch of optics revolving around experiments in which the quantized nature of the electromagnetic field is prominent. Quantum information, on the other hand, is the more theoretical equivalent of information theory. One of the experiments in which the electromagnetic field has to be described as being quantized is cavity quantum electrodynamics (CQED).

This thesis describes a CQED experiment involving electron spins trapped in quantum dots, which are themselves embedded in a cavity. The underlying goal is that of providing a physical way to construct a quantum computer, linking the project to the quantum information field. The aim of this project was to characterize and perform reflection measurements on polarization degenerate cavities. For this, control over the

1

degeneracy of the cavities is needed, which was done using the hole burning technique. Using polarization degenerate cavities, the final aim is to entangle the electron spins with photon polarization, such that the spins can serve as solid state storage qubits whereas the photons are a means of data transfer and manipulation.

1.1 Outline

This thesis has been written to be as useful as possible, in the hope that it might serve as a reference to future students. Too much detail has been omitted where possible, while still providing a complete summary. The following is a short overview of how this thesis is organized.

- The rest of this chapter continues with a basic introduction on (quantum) computers, since eventually implementing a quantum computer requires first an understanding of the building blocks. It describes the important quantum features that make the quantum computer unique with respect to the classical computer. The chapter continues with a general introduction to quantum dots and ends with a discussion on CQED.

- **Chapter 2** describes the experimental setup and the technical aspects of the samples. The second part of Chapter 2 focuses on the measurement techniques that toghether somewhat form a toolbox. The chapter ends with a brief description of the hole burning technique which is used to make the (fundamental mode of the) cavities polarization degenerate.

- **Chapter 3** presents the results of several different measurements, and follows the complete procedure on getting a cavity. All other results are presented here aswell, including the voltage-induced birefringence (electro-optical effect, the Pockels effect) and strain induced quantum dot spectral shifting. It contains a short section on the degradation of the samples, and the positioning samples are discussed.

- **Chapter 4** concludes with a short overview of the obtained results, and more importantly also gives a list of possible further (side-track) measurements to be considered.

- **Appendix A** gives a short overview of an attempt at modematching.

- **Appendix B** lists the most important files that were used during this project, either for the measurements themselves or for the analysis of the obtained data.

1.2 Information processing

A little introduction to the basics of information processing is needed at this point, to justify the goal of the experiment. The following will be a short outline of the most important aspects.

1.2.1 Bits

Normal (classical) computers use a **bit** as the fundamental data object. The bit is an entity that can have either of the values 0 or 1, and can hence be visualized as some sort of an 'on/off' switch. At the lowest level all data on a computer is stored as large collections of 0's and 1's (i.e. bits). Thus, using an entire array of such bits, any kind of data can be stored (Figure 1.1 gives an example). Physically, such a bit can be represented by transistors or magnetic strips. In the notation as is common in the information processing field (and quantum theory in general), let us denote the current state of the bit by the symbol $|b\rangle$. The states 0 and 1, in the same notation, are then represented by $|0\rangle$ and $|1\rangle$. Thus, in mathematical form there are the following two (mutually exclusive) situations for a classical bit:

$$|b\rangle = |0\rangle \quad \textbf{or} \quad |b\rangle = |1\rangle$$

If the value of the bit at a specific moment is not known deterministically (this is usually called a probabilistic bit), the state can be described by assigning a probability to the different values as in

$$|b\rangle = a|0\rangle + b|1\rangle$$

in which a is the probability for the bit to be in the $|0\rangle$ state and b the probability for the $|1\rangle$ state. Of course, the bit cannot be 'state-less', and so there is the condition that the sum of a and b has to equal unity.

```
01010001
01110101
01100010
01101001
01110100
```

Figure 1.1: All computer data is stored in binary format. The eight-bit (byte) strings each encode a character, which from top to bottom form the word `Qubit`*.*

Now consider a more general and much more interesting kind of bit, called a quantum bit (**qubit**). The general state of the qubit ($|qb\rangle$) is a superposition of both the $|0\rangle$ and $|1\rangle$ states

$$|qb\rangle = \alpha|0\rangle + e^{i\phi}\beta|1\rangle \tag{1.1}$$

in which the exponential factor represents a phase difference between the two states, the importance of which will be discussed below. Such a qubit state is conveniently described using a Bloch sphere as shown in Figure 1.2. Each possible qubit state can be visualized by a vector with its endpoint on the sphere. The coefficients α and β are then represented by the angle θ through $\alpha = \cos(\theta/2)$ and $\beta = \sin(\theta/2)$, and the angle ϕ is the parameter for the relative phase difference.
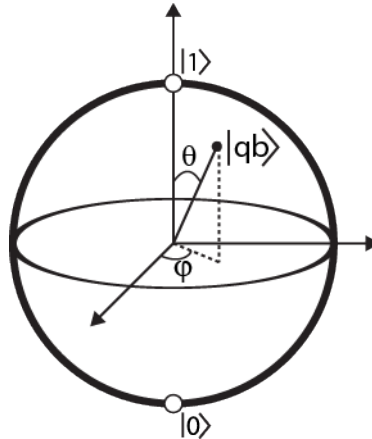
3

Figure 1.2: A Bloch sphere showing a single qubit state. All single qubit states can be represented by vectors lying on the Bloch sphere, where ϕ represents the relative phase between the $|0\rangle$ and $|1\rangle$ states.

If the two different states have a fixed phase relationship, the superposition is **coherent**. For the next section, consider a coherent superposition state given by

$$|qb\rangle = \alpha|0\rangle + \beta|1\rangle \tag{1.2}$$

This state resembles the probabilistic bit state, but it is very important to note the distinction between a qubit and a probabilistic bit. In the case of the qubit, α and β are *not* the probabilities for the qubit to be in the respective states. Rather, these probabilities are given by $|\alpha|^2$ and $|\beta|^2$ (satisfying $|\alpha|^2 + |\beta|^2 = 1$), since these coefficients are in general even comlex numbers. At first sight this would not seem to make any difference, until multiple (qu)bits are being considered. If two states are added together, apart from normalization the following situation arises:

$$
\begin{aligned}
|b_1\rangle &= a|0\rangle + b|1\rangle \\
|b_2\rangle &= c|0\rangle + d|1\rangle \\
|b_1 + b_2\rangle &= (a+c)|0\rangle + (b+d)|1\rangle
\end{aligned}
$$

The above shows that for this added state, the probabilty to measure $|0\rangle$ is just $(a+c)$ (apart from normalization again, the probabilities add). Now if the above states were qubit states the probability would not be simply $(a+c)$, but rather the absolute square of this, giving an extra $2ac$ term in the probability. This is a quantum inteference effect, which is an essential feature in quantum computation.

Another aspect to be considered is that it is not possible to predict the actual state of a qubit at a general moment. Only when the qubit is measured and the outcome is observed can it be said with certainty that the qubit is now in that measured state (after

the measurement, the time evolution of the state is given by the Schrödinger equation). This means that after the measurement the state of the qubit is no longer the general superposition; the qubit state has now *collapsed* into the measured state, and only the probability for the bit to collapse in either of the two states can be calculated beforehand. This behaviour is sometimes described as the qubit being a 0 and a 1 *simultaneously*. It 'decides' which of the values it becomes only when a measurement is made, but it is fundamentally impossible to predict the outcome. This effect is exactly what is made use of in quantum cryptography, since eavesdropping would hence destroy the superposition. Because the qubit is in both states simultaneously, performing a calculation on the qubit is also equivalent to performing the calculation on all possible states simultaneously.

The abovementioned interference effects only arise when the superposition is coherent, and this is why the relative phase is of such importance. To give an example of an interference effect, consider an electron spin in the state

$$\frac{1}{\sqrt{2}} \left(| \uparrow_x \rangle + | \downarrow_x \rangle \right)$$

Classically, this can be interpreted as the electron spin along the x-direction having a 50% chance of being directed towards the negative x-axis, and a 50% percent chance for being directed in the positive x-axis direction. If the spin along the z-direction were to be measured, classical theory would predict a 50% chance for up or down, *irrespective* of whether the spin is oriented along the positive or negative x-axis. If this were a quantum bit however, measuring the z-component of the spin would always result in spin up since the given state is nothing but the spin up state representation in the x-basis. In the end, this is the physical reason for why performing a computation on a single superposition of qubit states is the same as performing the computation on all possible classical bit states. To make this idea more clear, consider two classical bits for which there are four possible states:

$$|b_1, b_2\rangle = |00\rangle \quad \textbf{or} \quad |b_1, b_2\rangle = |01\rangle \quad \textbf{or} \quad |b_1, b_2\rangle = |10\rangle \quad \textbf{or} \quad |b_1, b_2\rangle = |11\rangle$$

all of which would have to be individually prepared. In contrast, all of these states can be represented by a single coherent superposition of a two qubit system as

$$|qb_1, qb_2\rangle = \alpha|00\rangle + \beta|01\rangle + \gamma|10\rangle + \delta|11\rangle$$

Continuing this until a computer of millions of bits is constructed, it is not hard to see where the (exponential) speed-up in computational power comes from. Actually, a quantum computer with only 64 bits is more powerful in such computations than any classical computer (because this qubit would describe a superposition that can represent $2^{64} \approx 1.8 \times 10^{19}$ different classical bit states simultaneously).

Physical implementation

The biggest problem today with qubits is their physical representation. A qubit can be represented by any so called two-level system. A two-level system is a system with

two distinct states, to which we can arbitrarily assign the labels 0 and 1. Examples to guide the mind are the two orthogonal polarization states of a photon, or the spin up and spin down configurations of electron spins. Various approaches are being used by different research groups. Two of the most represented approaches are trapped ions [3] and electron spins [1]. Each of them has its own (dis)advantages. Briefly, trapped ions are easier to manipulate and harder to scale, whereas the opposite is true for the electron spins.

The experiments that are being done using trapped ions as qubits rely on the electronic state of the ion as a two-level system. For example, the hyperfine splitting of the ions can be used to represent such a system. Although reading and preparing the electronic states of ions is not the hardest part of the experiment, the difficulty arises in trapping multiple ions and have them interact. This is in itself not a problem for a few ions, but if one wishes to scale this system, more and more tricks (such as 'shuttling' the ions from trap to trap [9]) are needed.

The experiment for this thesis focusses on electron spins, which are trapped using quantum dots (section 1.3). The fabrication of the quantum dots is under control, but it is difficult to manipulate single electron spins. To increase the ease of interaction with the electron spins, the quantum dots are themselves embedded in a semiconductor cavity. An extra difficulty is that in contrast to the trapped ions, the electron spins are completely surrounded by (nuclear) spins present in the environment, causing decoherence.

1.2.2   Algorithms

Supposing that a working array of quantum bits (i.e. a quantum computer) has been constructed, it is now possible to perform various operations on the qubits. The algorithms that use these operations are different from their classical counterparts, since they have to be compatible with quantum theory [14]. Hence the development and optimization of quantum algorithms has turned into a separate field by itself. Well known algorithms are for example Shor's factorization algorithm (to factorize prime numbers, as mentioned earlier) or Grover's algorithm for searching databases (which provides a quadratic speed-up rather than exponential). An important thing to note is that most quantum algorithms are probabilistic, in the sense that they do *not* always provide the correct answer. Simply repeating the algorithm increases this fidelity. An example of a non-probabilistic (i.e. deterministic) quantum algorithm is the Deutsch-Jozsa algorithm (with little practical use).

A very important aspect of quantum algorithms is that the operations that are performed on the qubits have to be **unitary**, meaning that the operations do not project or collapse the state of the qubit. This in turn means that measuring the state of the system using these operations is not possible. In terms of the Bloch sphere, unitary operations are those operations that leave the length of the state vector unaltered. The action of unitary operation can therefore be visualized as a simple rotation of the state

vector, making sure that the result is still a vector on the Bloch sphere (and hence a valid qubit state).

These operations are more easily performed on photons than on the electron spins directly. The two systems (electron spin and photon polarization) are therefore coupled through entanglement (see section 1.4). This implementation is called **hybrid**, since two different physical systems are being used. In short then, the aim is to use **solid state qubits** (electron spins in quantum dots) for storage of information, and to use photons to tranfer data and perform the manipulations on.

1.3 Quantum Dots

A quantum dot is sometimes called an artificial atom. The reason for this is that the quantum dot, just like an atom, has a confining potential in three dimensions giving it discrete energy levels. As a result it can confine electrons (and holes), giving it interesting properties for a large variety of applications such as LEDs, solar cells and diode lasers. As will be described in the following, the quantum dots also provide a way to implement qubits. A nice explanation of quantum dots can be found in [24] and [15].

1.3.1 Growth

The growing of the quantum dots starts with a GaAs substrate. By depositing single layers of InAs on top of this substrate, there is a formation of small islands of InAs. This formation of islands occurs because of a slightly different value for the crystal lattice constant of InAs as compared to GaAs. The first layer does not 'fit' on top of the substrate perfectly, and experiences some strain. By adding more layers (until a critical thickness is reached), the InAs starts lumping together to form the dots. This fabrication process is called the **Stranski-Krastanov** growth method. Figure 1.3 shows an AFM image in which the dots are clearly visible.

The typical dimension of the dots is about 25 nm in the plane (approximately circular), and about 2 nm in the direction normal to the plane (which from now on shall be the z-direction). The concentration of dots throughout the sample varies, and can be controlled during growth. The concentration cannot be too high however, since the dots would then start perturbing each other. The layer of quantum dots is then capped off with another layer of GaAs to match the fundamental mode of the cavities. This layer of material will be referred to as the **active layer**.

1.3.2 Band structure

The bandgap of the dots (InAs) is slightly smaller than the bulk (GaAs) in which they are embedded. This gives the quantum dot a confining potential that is like a quantum well in the z-direction and parabolic in both the x- and y-direction. Electrons and holes
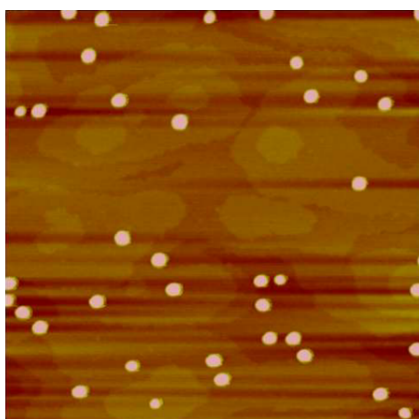
Figure 1.3: AFM image of uncapped layer of InAs quantum dots. The area of this image is 1µm by 1µm. Courtesy Antonio Badolato. (Image taken from M. Rakher's thesis [22]).

that are excited at or near the dot can hence be trapped. A qualitative picture of the local energy structure (in the z-direction) in the vicinity of a dot is shown in Figure 1.4.
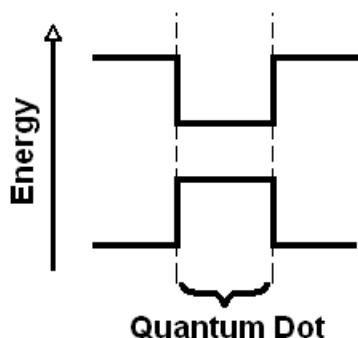

Figure 1.4: Band structure of the z-direction near a quantum dot. The bandgap of the quantum dot is smaller than that of the environment, and so provides an effective trap for electrons and holes. Figure 1.6 provides some more detail.

The trapped electron spins can then be used as our qubit, since this spin has two possible states and hence is a two-level system.

A bit more can be said on the bandstructure of the surrounding GaAs, following partially the section on the physics of quantum dots as found in [24]. Detailed information on quantum dots and specifically on semiconductor physics can for example be found in [28].

8

The electrons in a solid experience a periodic potential due to the periodic lattice of the material, affecting their movement. This periodicity is reflected in the wavefunction for the electrons:

$$\psi_e(\vec{r}) = e^{i\vec{k}\cdot\vec{r}}u(\vec{r})$$

in which $u(\vec{r})$ is a function with the same periodicity as the lattice (i.e. $u(\vec{r}+\vec{R}) = u(\vec{r})$, with $\vec{R}$ any lattice vector) and where $\vec{k}$ is the electron's wave vector. In the case of a slowly varying potential in a direct-gap semiconductor, the electron wavefunction is often approximated as

$$\psi_e(\vec{r}) = f(\vec{r})u(\vec{r})$$

in which $f(\vec{r})$ can be seen as the enveloppe of the wavefunction, satisfying Schrödingers (time-independent) equation with potential $V(\vec{r})$:

$$\left[-\frac{\hbar^2}{2m^*}\nabla^2 + V(\vec{r})\right]f(\vec{r}) = Ef(\vec{r})$$

The m^* appearing in the Hamiltonian is the effective mass of the electron. If the motion is one dimensional, and the electron experiences a periodic potential with no a-periodic perturbations, the effective mass can be calculated via

$$m^* = \hbar^2 \left[\frac{\partial^2 \epsilon(k)}{\partial k^2}\right]^{-1} \tag{1.3}$$

in which $\epsilon(k)$ is the dispersion relation, giving the energy ϵ as a function of the wave vector k. In general, the effective mass is different from the actual mass of the electron. In the special case of free electrons ($V(\vec{r}) = 0$), the dispersion relation is quadratic in k. This can easily be derived by noting that a free electron only has kinetic energy, and so using the de Broglie relation ($p = \hbar k$) the Hamiltonian can be written as

$$H = \frac{p^2}{2m} = \frac{\hbar^2 k^2}{2m}$$

where m this time is the actual mass of the electron. The energy eigenvalues obtained from this Hamiltonian are hence simply given by

$$\epsilon = \frac{\hbar^2 k^2}{2m}$$

which is exactly the needed dispersion relation. By subsititing this relation into equation 1.3 the effective mass of a free electron is found to be $m^* = m$, which was to be expected since the electrons motion is not affected by any potential.

Qualitatively then, from equation 1.3, the curvature in the plot of energy versus wave vector is a measure for the mass of the particle. Figure 1.5 shows the energy diagram for GaAs. Notice the different curvatures for the holes, which have hence been divided into **heavy** holes (HH) and **light** holes (LH). Apart from a different effective mass, they are different in spin as well.
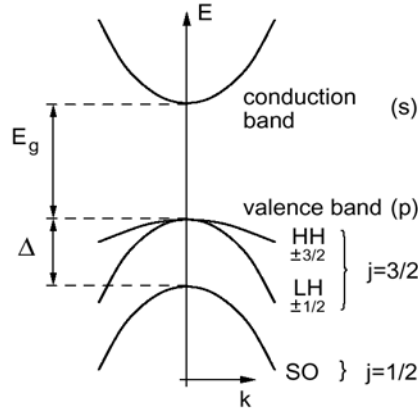
Figure 1.5: Band structure of GaAs. The energy depends quadratically on the wave-vector k, while the prefactor is a measure for the effective mass of the particles. The heavy holes (HH) and light holes (LH) have different spin, but are degenerate in energy at $k = 0$. This degeneracy is lifted by size quantization and strain in the sample. The spin-orbit (SO) band is neglected due to the large energy difference with the HH band. Image taken from [28].

Due to the size quantization (and strain in the structure), the degeneracy between light holes ($\pm\frac{1}{2}$ spin) and heavy holes ($\pm\frac{3}{2}$ spin) at $k = 0$ is lifted (not shown in the figure). There is also a spin-orbit (SO) band visible in the figure, which will not be considered in the rest of this thesis because it can be neglected due to a large energy difference.

The band structure of to the quantum dots as shown in Figure 1.4 gives rise to multiple energy levels. This is analogous to the confining potential of an atom, giving it properties such as discrete energy levels. The lowest energy level of the dot (similar to an S-type atomic orbital) can hold two electrons, and the lowest energy level for the holes is able to hold two (heavy) holes (see Figure 1.6). It is the electron-hole pairs in which the holes are heavy that are studied here.

1.3.3 Charged states

The quantum dot layer is placed on a PIN-diode like structure, allowing the quantum dots to be in different charged states by applying a bias voltage. The effect of the bias voltage is that the energy of the p-type region of the PIN-diode is lowered with respect to the n-type region. Since the Fermi-level is unaffected, the quantum dot energy well drops below the Fermi-level. Depending on the voltage, single electrons can hence occupy the quantum dot levels. The state in which a single electron is occupying the quantum dot (giving it a negative charge) is denoted X^- and is called the **trion** state. The above is shown in Figure 1.7.

Consider now a quantum dot in the singly charged trion state. The spin of this
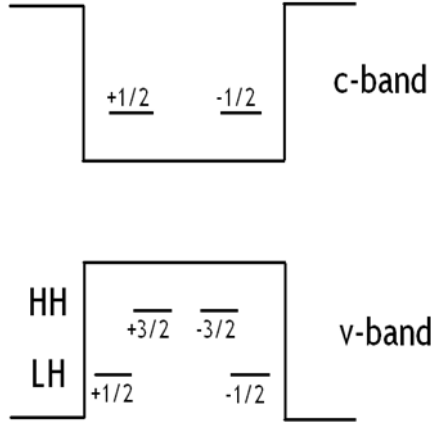
Figure 1.6: The energy levels of the quantum dot. The heavy holes and light holes have different energies due to the strain and size quantization.

(a) No applied voltage
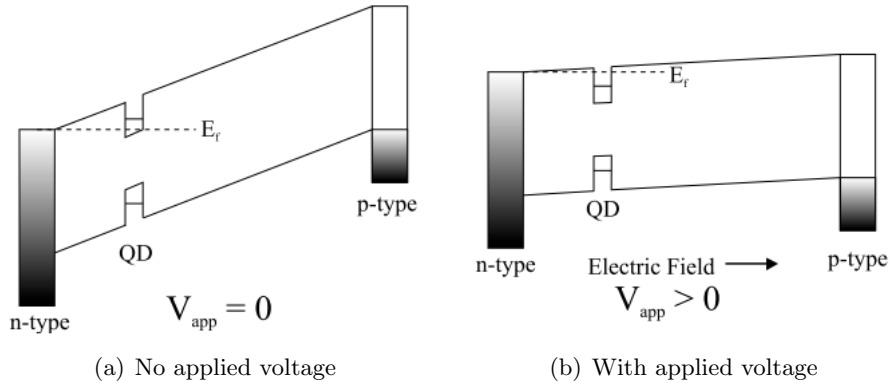
(b) With applied voltage

Figure 1.7: The sample behaves like a PIN diode. (a) Without applying a voltage, the p-type region is higher in energy than the n-type region. (b) With a voltage, the p-type region can be energetically lowered with respect to the n-type region. This in turn charges the dot, since its energy levels drop below the Fermi-level E_f. (Images taken from M. Rakher's thesis [22]).

electron is either up ($\uparrow$) or down ($\downarrow$). Depending on this spin, either of the following two situations occurs when an electron-hole pair is created and trapped:

$$| \uparrow \rangle \rightarrow | \uparrow \downarrow \Uparrow \rangle$$

or

$$| \downarrow \rangle \rightarrow | \uparrow \downarrow \Downarrow \rangle$$

where $\Uparrow$ and $\Downarrow$ denote the heavy hole spin. In both of the cases, the two electrons in the trion state form a singlet state. This means there is no spin-orbit interaction.

11

1.3.4 Selection rules

The two abovementioned situations are bound to selection rules. The photons considered here have no angular momentum and so only have spin ($S_z = \pm 1$). The two different circular polarization states will from now on be labelled $|L\rangle$ for $S_z = -1$ and $|R\rangle$ for $S_z = +1$. Conservation of total angular momentum means that a photon in the $|L\rangle$ state can only create an electron-hole pair in which the electron has spin $+\frac{1}{2}$ and the hole $-\frac{3}{2}$. The same reasoning holds for the $|R\rangle$ photon. These **optical selection rules** for the trion state are displayed in Figure 1.8.
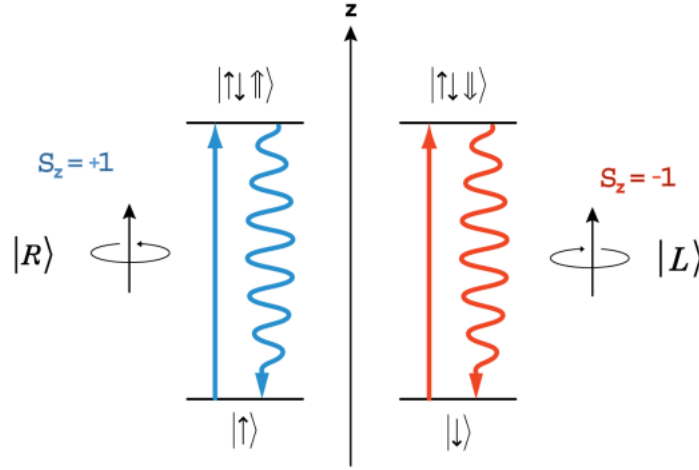

Figure 1.8: The optical selection rules for the trion state. Angular momentum has to be conserved, and so an $|R\rangle$ state photon (with $S_z = +1$) creates an electron (heavy) hole pair in which the electron has spin $-\frac{1}{2}$ and the hole $+\frac{3}{2}$. If there is already an electron present with spin $-\frac{1}{2}$, the $|R\rangle$ state photon is unable to create an electron-hole pair.

One other property of the trion state regarding selection rules, is that there is always an electron available for the hole to recombine with. Therefore this state is also called a **bright state**. On the other hand, the neutral state (a quantum dot with no extra trapped electron) can have a **dark state**. This is possible since there is a possibility for the electron to flip its spin when trapped (due to perturbations), after which the electron and hole are no longer able to recombine. Notice also that the light that is emitted by the quantum dots is hence circularly polarized, following the same selection rules depending on the electron spin.

1.3.5 Photoluminescence

The recombination of the electron-hole pairs does not necessarily take place through the quantum dots. It is actually even more unlikely to excite electron-hole pairs directly at

the dot. Instead, most of the pairs are excited in the GaAs surrounding the dots. The pairs then either migrate towards the dots and recombine there, or recombine outside the dots. As long as the pump intensity is not too high (and by that is not creating too many electron-hole pairs), the emission of the GaAs does not dominate over the emission of the quantum dots. This emission by recombination of electron-hole pairs is called photoluminescence, since they were excited using light. Figure 1.9 summarizes the above.

(a) Excite electron-hole pair above bandgap

(b) GaAs recombination
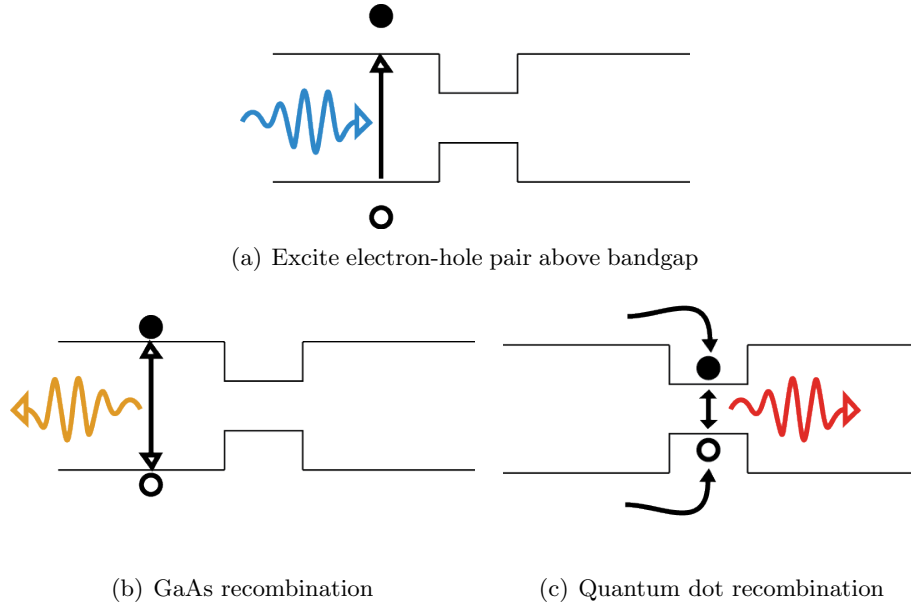
(c) Quantum dot recombination

Figure 1.9: (a) An electron-hole pair is excited by pumping with an above-bandgap laser (blue). (b) If the electron-hole pair does not diffuse to a quantum dot, they recombine over the GaAs bandgap (orange). (c) If the electron-hole pair gets trapped, they recombine through the quantum dot (red). The light used and observed in the experiment does not have the same wavelength as shown here.

1.4 CQED

Cavity quantum electrodynamics studies the interaction between a quantum system (e.g. an atom) contained in a cavity and a single mode of the quantized electromagnetic field. The cavity serves both to confine (and quantize) the field and to enhance the interaction between the photons and the quantum system. The quantum system used here is a quantum dot, which for the rest of this section will also be referred to as a dipole. The quantum dot can be referred to as a dipole because the trapped electrons and holes are spatially separated, giving the quantum dot a dipole moment.

Section 1.3 described the quantum dots, and showed that we can treat them as a two-

level system. The interaction between the cavity and the two-level system are then mathematically described by the **Jaynes-Cummings** model [12]. A representation of the eigenstates of the quantized electromagnetic field is through the **Fock states**, also called **number states**. In this representation the number of photons in the field mode is known, and the mathematical notation for such a state with n photons is $|n\rangle$. The Jaynes-Cummings model predicts that (in the ideal case) the two-level system and the electromagnetic field inside the cavity undergo vacuum Rabi oscillations, in which the electromagnetic field continuously exchanges a single photon with the two-level system (which in turn continuously switches between its groundstate $|0\rangle$ and its excited state $|1\rangle$). In other words, the emission of the dipole is *reversible*, unlike in the situation in which the dipole would radatiate into free space. Symbollicaly, these Rabi oscillations can be described by

$$|0\rangle|n\rangle \leftrightarrow |1\rangle|n-1\rangle$$

In practice however, the efficiency of these oscillations depends on the two-level system and the cavity, as will be discussed in the next subsection. Even more important to take into account is the interaction between the cavity-dipole system and the light used to probe it.

1.4.1 Coupling regimes

The interaction between the cavity, quantum dot and the electromagnetic field is described in any quantum optics book (for example, see [11]), and can be characterized by three parameters (see also Figure 1.10):

- g: The dipole-field coupling

- κ: The cavity decay rate

- γ: The dipole decay rate

Based on the ratio's of these parameters, either of two coupling regimes is possible. These regimes are the **strong** and **weak** coupling regimes.

Strong coupling

In the strong coupling regime, $g > \kappa$ and $g > \gamma$. This means for example that a photon emitted by the quantum dot is likely to be re-absorbed again instead of escaping the cavity. This is of course just what is described by the Rabi oscillations. Most of the proposed quantum information processing algorithms make use of the strong coupling regime, but it is difficult to reach strong coupling experimentally.

Weak coupling

The weak coupling regime is characterized by the parameter relation $\kappa > g$ (this is sometimes also called the "bad-cavity" regime). It is also assumed that the incoming
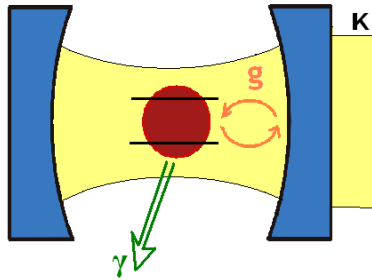
Figure 1.10: Schematic of a cavity with quantum dot inside. The various interaction parameters are denoted g, κ and γ. The represent the dipole-field coupling, cavity decay rate and dipole decay rate respectively.

field for excitation is weak, in order to keep the quantum dots in the ground state (on average). In the weak coupling regime the chance for an emitted photon to be re-absorbed is small. This does not mean at all that there are no interesting effects, nor does it mean that this regime is useless for quantum information processing [4]. The main effect in the weak coupling regime is the modification of the spontaneous emission rate, also called the **Purcell effect** [20]. The spontaneous emission rate depends linearly on the density of states, as given by **Fermi's golden rule**. The density of states increases with decreasing cavity volume. This effect is contained in the abovementioned dipole-cavity coupling factor g, given by

$$g = \sqrt{\frac{e^2 f}{3 m_0 n_{\mathrm{eff}}^2 \epsilon_0 V_{\mathrm{eff}}}}$$

which shows indeed that decreasing the (effective) cavity volume V_{eff} increases the coupling factor. The other parameters are material properties, except for f, which is the oscillator strength and is proportial to the square of the dipole moment of the quantum dot.

Instead of the coupling factor g it is common to use another figure of merit, the **Purcell factor** F_P [20]. It is the ratio of the emission rate of an atom in a cavity to that of an atom in free space. Introducing also the quality factor Q of a cavity[1], the final form of the Purcell factor can be stated as:

$$F_P = \frac{3}{4\pi^2} \left(\frac{\lambda}{n}\right)^3 \frac{Q}{V_{\mathrm{eff}}}$$

Again the important aspect is the factor Q/V_{eff}, giving the Purcell factor an inverse dependence on the cavity volume. Another parameter describing the coupling efficiency

---

[1] The quality factor is a measure of the optical confinement and the loss-rate κ of the cavity $(Q \sim \frac{1}{\kappa})$.

is the Q appearing in the Purcell factor. Usually, the two coupling regimes are distinguished not by the values of g, κ and γ, but by either 'high' (for strong coupling) or 'low' (for weak coupling) Q values.

1.4.2 Dipole-induced reflection

The experiments described in the rest of this thesis are all in the weak coupling regime. Upon probing the cavity with a weak field, there are two possible scenarios [27],[25]. Consider first the excitation of an atom in free space, as shown in Figure 1.11(a). Since the atom emits radially in every direction, there is little interference between the excitation laser and the atom's emission. The effect is also observed if the atom is not coupled to a cavity mode, and hence can be considered to be in free space. Now consider an atom that *is* coupled to a cavity mode, as in Figure 1.11(b). The image shows a single cavity mode and an atom, and assumes the system has a high Purcell factor F_P such that the atom is coupled to the cavity mode. This means 'all' of the emission of the atom is in the cavity mode (there are of course some losses), and it is therefore obvious that there is noticable interference between the probing light and the atom's emission.

(a) Atom in free space, **uncoupled**   (b) Atom **coupled** to a cavity mode
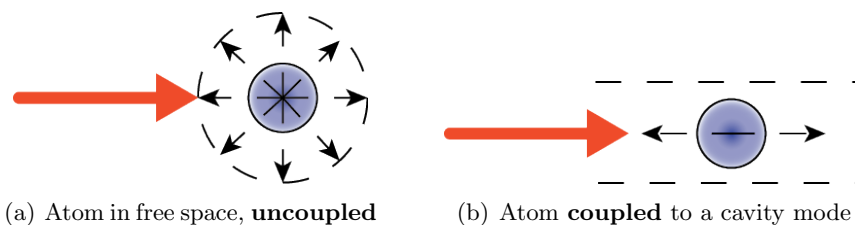
Figure 1.11: (a) An atom in free space (or an atom that does not emit into a cavity mode) has little interference between its emission and the probing light. (b) If the atom is in a cavity and the system has a high Purcell factor F_P, most of the atom's emission is in the cavity mode. In this case, there is interference between the probing light and the atom's emission.

The above described two situations (i.e. coupled and uncoupled) have a clear effect when looking at the system's reflection as a function of frequency. Whether the atom is coupled or uncoupled depends on the frequency of its emission and the resonance frequency of the cavity. In the uncoupled case, the atom is not on resonance with the cavity mode, and there are little or no interference effects. The reflection curve hence only shows a reflection dip at the resonance frequency of the cavity (see Figure 1.12(a) and the red (uncoupled) curve in Figure 1.13). In the coupled situation, the interference between the probing light and the atom makes the cavity reflective (Figure 1.12(b) and the blue (coupled) curve in Figure 1.13).

Entanglement

The dipole-induced reflection and the selection rules together allow for spin-photon entanglement. If the spin is in a general superposition $\alpha|\uparrow\rangle + \beta|\downarrow\rangle$ inside the cavity, then

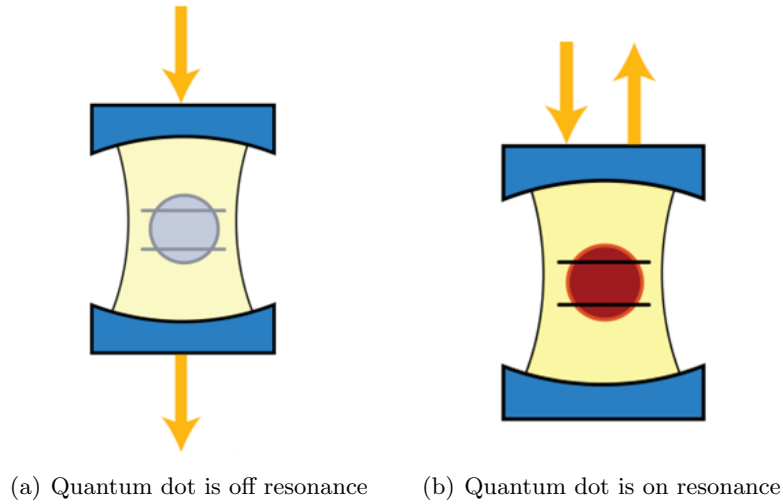(a) Quantum dot is off resonance   (b) Quantum dot is on resonance

Figure 1.12: (a) If there is no quantum dot on resonance, the cavity transmits the light at that frequency. (b) If there is a quantum dot on resonance, the interference between the incoupled light and the light emitted by the quantum dot makes the cavity reflective.
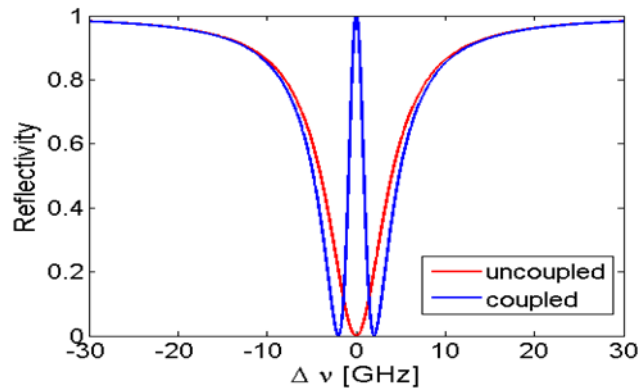

Figure 1.13: The reflection curves for the coupled and uncoupled situations. If the dot is coupled (on resonance) with the cavity, the light is absorbed and the cavity becomes reflective. Without a dot on resonance, there is only a transmission dip. In a real experiment, the reflection peak will not go up to 100% reflectivity due to losses in the optical system. Because of the two spin states, the maximally achievable visibility is just below 50% unless there is selective spin pumping. (Image taken from M. Rakher's thesis [22]).

by pumping with $|R\rangle$ polarized light the situation as shown in Figure 1.14 arises. The polarized light in the $|R\rangle$ state is unable to act on the $|\downarrow\rangle$ spin, and so the cavity is effectively transmissive in this situation. If the spin is in the $|\uparrow\rangle$ state however, the

light gets absorbed and re-emitted. The re-emitted light has reversed direction and so is perceived as polarized in the orthogonal $|L\rangle$ state. The global state of this system can then be given by

$$|\Psi\rangle = \alpha|L\uparrow\rangle - \beta|R\downarrow\rangle$$

The minus sign arises because of a phase shift due to reflection. This is an entangled state, since this wavefunction cannot be decomposed into the product of the wavefunctions of the spin and photon separately. If the polarization of the photon was now measured to be $|L\rangle$, the spin state would instantly become $|\uparrow\rangle$ since this measurement projects the state into $|L\uparrow\rangle$.
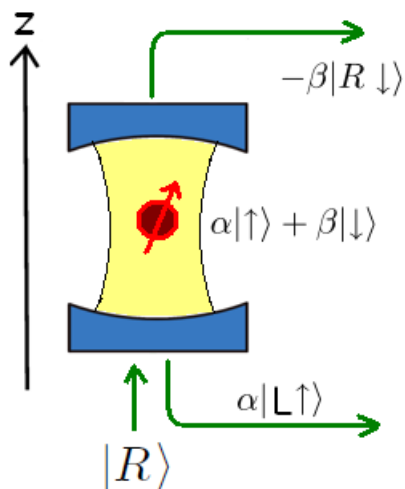

Figure 1.14: Creating an entangled state by pumping with $|R\rangle$ polarized light. The part of the spin state on which the photon cannot act (selection rules) contributes to a transmissive part (with phase shift due to reflection), while the other part is represented by a reflection as orthogonally polarized light.

1.4.3 Polarization degeneracy

Finally, one of the most important aspects to mention in this thesis is the need for polarization degenerate cavities. By polarization degenerate cavities, it is from now on ment to actually indicate a polarization degenerate fundamental mode (since the fundamental mode is the easiest to couple to). The fundamental mode of the cavity is initially non-degenerate (due to fabrication, see section 2.2.1), it is actually split into two peaks differing in frequency.

This splitting arises because of asymmetry and strain in the semiconductor material. The effect is known as birefringence, and has as its fundamental cause a differce of refractive indices of the material in two orthogonal directions. More details on this follow

in section 2.3.4 on hole burning.

The importance in making the fundamental mode polarization degenerate lies in two separate reasons:

- Since measuring the polarization of the emitted light is (through entanglement) equivalent to measuring the spin state of the electron, this measurement would project the spin into the measured state. In order for quantum algorithms to work, this projection should not take place since it destroys the superposition. Another way to put this, is by noting that the superposition states should be indistinguishable. Since the quantum bit is (again, through entanglement) the two-level polarization of the photon, it must not be possible to measure the polarization in any other way. If the cavity is non-degenerate, the polarization can simply be obtained via the frequency of the emitted light.

- The second reason is a more practical one. In the end one wishes to address the electron spin qubits simultaneously (using a narrow bandwidth laser). This would not be possible if the frequency splitting between the two states is larger than the bandwidth.

The route to getting the cavity polarization degenerate, is by changing the strain in the cavity. This can for example be done by applying pressure to the sides of the sample [7]. The method that is used here, is by creating small defects in the cavity by burning with an intense laser beam (see section 2.3.4 and [5]). Since the quantum dot emission has a bandwidth of about 2GHz, the cavity is considered to be polarization degenerate if the splitting in frequency is **less than 2GHz**, or (equivalently) **less than 0.06nm** in wavelength.

Chapter 2

Experimental

This chapter describes the experimental setup, the samples and explains the measurement techniques. The section on the measurement techniques can be regared as a 'toolbox', with which the results as described in the next chapter are obtained.

2.1 Experimental Setup

The experimental setup can roughly be divided into three major parts. They are the **optical table** including optical elements, the **cryostat**, **lasers** and **detectors**.

2.1.1 Optical table

Figure 2.1 shows a schematic view of the optical table. For doing photoluminescence measurements (e.g. spectra, stark shift and spatial scans), mirror **A** is taken out and the 780nm diode laser reaches the sample. The **CCD** (charge coupled device) is used to image the cavities for rough alignment. When aligned, beamsplitter **BS 2** is taken out since the CCD is no longer needed. This doubles the power reaching the sample. In order to burn holes mirror **A** is put back in, while beamsplitters **BS 1** and **BS 2** are taken out (to prevent damage to other optics). Before the hole burning actually takes place, **BS 2** is still in (but with low laser power) to use the CCD for positioning the burn-spot. Finally, to do reflection measurements, a tunable 938nm Velocity laser is coupled in from the spectrometer path. By taking out mirror **B**, this laser reaches the (avalanche) photodiodes after relfecting from the sample in the cryostat.

2.1.2 Cryostat

Figure 2.2 is a schematic view of the inside of the cryostat. On the bottom right is the inlet for the helium flow. The helium flows through another tube (not shown in the image) and then enters a set of coils designed to cool the system. The yellow dots are the windings of these coils, as seen from the front. First, the helium enters the coils
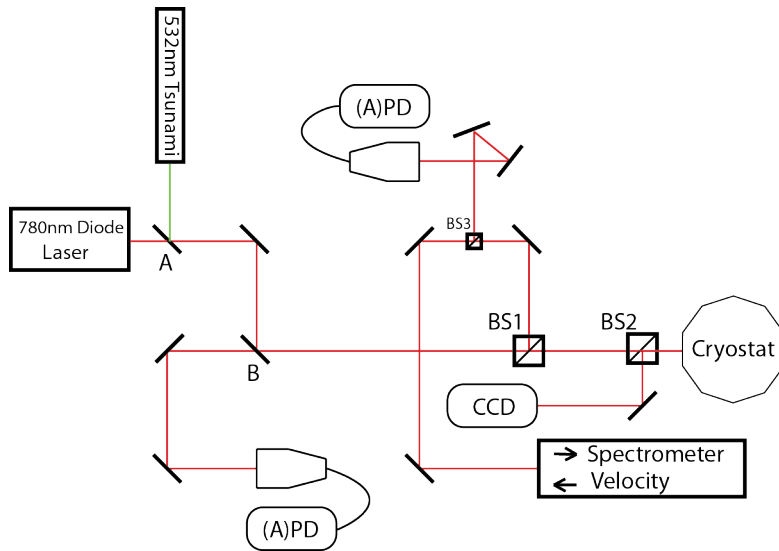
*Figure 2.1: A schematic view of the optical table. With mirror **A** out and **B** in, the 780nm diode laser can be used to image the sample and do photoluminescence measurements. To do hole burning, mirror **A** and **B** are put into place, but **BS 1** and **BS 2** are taken out in order to avoid damage to other optical components. Last but not least, mirror **B** and **BS 2** can be taken out to do reflection measurements. A tunable 938nm Velocity laser is then sent in from the spectrometer path, and this laser reaches both (avalanche) photodiodes after being reflected from the sample.*

directly beneath the 4K pot, and then spirals outwards through the yellow coils (vertically aligned dots) cooling the 60K pot. From there, the helium flows into the return line. The 4K pot is connected to the sample holder and the attocubes. The sample itself is on top of the sample holder, and usually reaches a temperature of about 5K. The attocubes (which are just piezo-electric crystals) are three stacked cubes, designed to move the sample in the x-, y- and z-directions. Also not shown in the image, is another connection to the cryostat that is used for a vacuum pump. During operation, the pressure inside the cryostat ranges from 5×10^{-8} to 4×10^{-7} mbar. The final crucial part in the cryostat is the PI-stage, which is used to independently move the objective.

The attocubes are used to move the sample into focus and adress different cavities. They hence provide rough alignment. Using the attocubes, an accuracy of about 10nm (at 4K) is reachable. For higher accuracy it is also possible to move the objective instead of the sample, using the PI-stage. The PI-stage reaches an accuracy of 0.3nm, and has a range of $100\mu m$ in both the x and y directions.
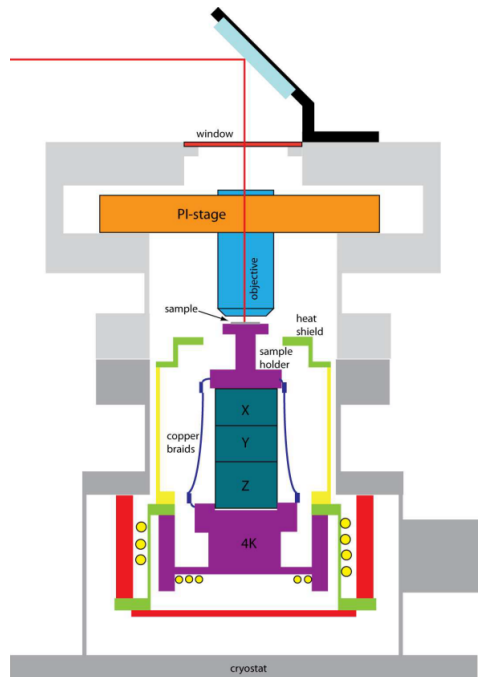
Figure 2.2: A schematic view of the cryostat. The liquid helium flows through the yellow coils and first cools the 4K pot. The 4K pot is in contact with the attocubes and sample holder, which hence also get cooled. The sample has a typical temperature of about 5K during operation.

2.1.3 Lasers & Detectors

There are three different lasers that are used in this setup. One of them is a diode laser used for photoluminescence and imaging of the cavities. It has a wavelength of 780nm, which means it pumps above bandgap. The second laser is a green (532nm) Ti-Sapphire **Tsunami** ring laser, which is used for burning holes and doing lifetime measurements. It has an external pump laser, providing a maximum power output of 5W. For alignment on hole burning however, the output is set to 200mW, and an additional OD4 filter is inserted (attenuating by a factor 10^4). This means the power reaching the sample is in the μW range. The actual hole burning is done at 500mW with no extra OD filters. The Tsunami laser can also be made to operate in a 20ps pulse mode. This mode is needed to do lifetime measurements on the quantum dots, to distinguish between the various charged states (section 1.3.3). Finally, a tunable external cavity laser (Velocity) centered around 938nm is used to do reflection measurements.

Spectrometer

The spectrometer used is a Horiba Jobin Yvon high resolution spectrometer, with a Horiba grating. The CCD camera together with the grating allow for a resolution of 0.016nm per pixel (equivalent to 5.5GHz per pixel). The spectrometer has a total range of about 17nm (or 5.6THz), since the camera has 1024 pixels.

Photodiodes

The photodiodes (PD) are used for reflection measurements. Two photodiodes are used for alignment and optimization of the relfection signal. One of them provides a reference signal to which the final signal is normalized. Once the reflection dip is seen and optimized, the non-reference photodiode is replaced by a femtowatt receiver. This photodiode is much more sensitive to lower powers, which is needed since the relfection peak from the quantum dots is only visible at very low powers (see also section 3.6). For even higher sensitivity, both the femtowatt reciever and the reference photodiode can be replaced by avalanche photodiodes (APDs). These photodiodes are extremely sensitive to light, since they have a bias voltage applied that is *just* on the threshold of the diode breakdown voltage. The smallest intensity reaching the APD makes it cross the breakdown voltage, and the result is an avalanche of electrons. An internal circuit stops this avalanche and prepares the APD for the next breakdown. The period of stopping and preparing is called the dead-time of the APDs, and is on the order of nanoseconds.

2.2 Samples

The layout of the cavities on the sample is discussed in this section. A more detailed description of the cavities themselves is provided first, starting with the cavity fabrication [18].

2.2.1 Cavities

The cavities serve to confine the light around the quantum dot, and impose boundary conditions that enhance the quantized nature of the light. The spontaneous emission rate of the quantum dots depends inversely on the cavity mode volume (see section 1.4.1), and hence by creating small cavities the emission can be greatly enhanced.

Fabrication

The cavities are the last step in the sample fabrication. Up to this point, the sample consists of the active layer, sandwidched between Distributed Bragg Reflectors (DBRs). The DBRs consist of alternating $\frac{1}{4}\lambda$ thick GaAs and $Al_{0.9}Ga_{0.1}As$ layers, and effectively form a Fabry-Perot-like mirror structure. Due to these DBR structures, there is already confinement of the light field in the z-direction (which is taken to be perpendicular to the active layer). To create confinement in the x, y-plane (i.e. the active layer) in which the

dots are situated, a way to access this layer through the DBR mirrors is needed. To this end, **trenches** are etched into the structure as is shown in Figure 2.3. It is important to note that the whole procedure for fabrication of the sample is a "bottom-up" process:

- First the bottom DBR structure is grown, consisting of 32 alternating layers.

- On top of that is where the active layer is grown.

- Then the top DBR structure is grown, consisting of 23 alternating layer.

- Finally, the trenches are etched for the oxidized aperture (see below).

Figure 2.3: Image of a single cavity as seen from the top. The trenches are etched through the upper DBR, the active layer and part of the lower DBR.

These trenches reach through the top DBR structure, and continue even a bit into the lower DBR structure. Once etched, the trenches allow for growth of an aluminum oxide aperture. The oxide grows inwards from the trenches, and the resulting aperture leaves open an approximately circular central region (the active area) of about 2 to 3μm in diameter. That this aperture is not perfectly circular is due to both asymmetries in the placement/dimensions of the trenches, and the anisotropic growth-rate of the oxide (this was done on purpose). Figure 2.4 shows the sideview of a cavity with oxidation layer.

This means we now have a complete cavity with an active layer of quantum dots. Of course, there are also electrical contacts in the sample which I have omitted to mention. The exact details can be found in M. Rakher's thesis [22]. Last but not least, there is a need to mention the position of the cavities. The samples that were used for the largest part during this project, had cavities that were arbitrarily positioned. That is to say, they were not centered on a dot. This was simply because the concentration of dots is high enough to make sure there is always at least one dot near the center. Section 3.9.1 discusses another approach for cavity placement.

Cavity modes and spectrum

Modes

The cavity with aperture now confines light in all three spatial dimensions. A simple but accurate model then describes the cavity as a quantum well in the z-direction, and
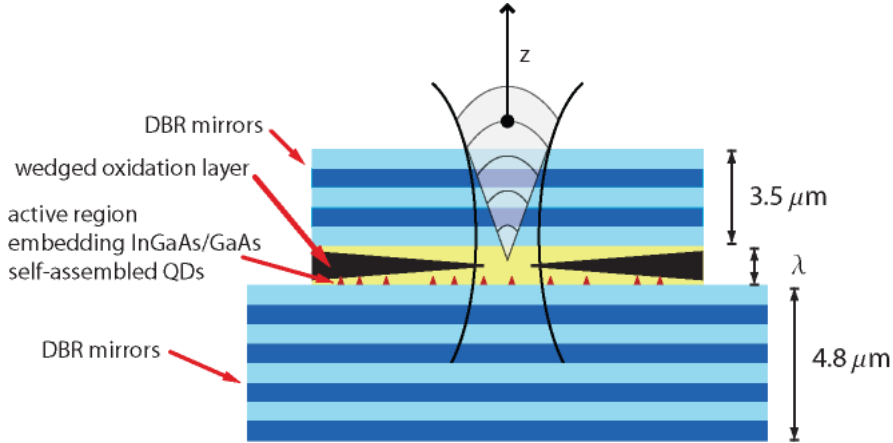
24

Figure 2.4: Slice-through of a cavity. The wedged oxidation layer is shown, together with the active layer and the dots. Both of the DBR structures have also been indicated.

as a parabolic potential due to the aperture in both the x- and y-directions. The modes of a parabolic potential are Hermite Gaussian modes[1]:

$$\Psi_{\mathrm{nm}}(x, y) = H_n(x)\, H_m(y)\, e^{-(x^2/\omega_x^2 + y^2/\omega_y^2)} \tag{2.1}$$

These modes have been experimentally verified [10] for the lower orders. Higher order modes are expected to deviate (to Laguerre Gaussians) since the parabolic potential flattens. Figure 2.5 shows a few of the modes.

Spectrum

The spectrum of the cavities follows the simple formula

$$\lambda_{\mathrm{nm}} = \lambda_{00} - an - bm \tag{2.2}$$

in which λ_{00} is the fundamental mode wavelength, and where a and b are parameters related to the size of the modes in the x and y directions respectively. They can be used to obtain information about the size of the fundamental mode, which is further discussed in section 3.1. An example of a spectrum with indicated labels for n and m can be seen in Figure 2.6.

The image shows the spectra taken with two orthogonal polarizations (black and red curves). Notice that the λ_{00} peaks do not overlap, and so this cavity is not polarization degenerate. The spectrum taken without any polarizers would be the sum of the two curves.

---

[1]The actually observed pattern is of course the square of this function.

25

(a) The fundamental mode, $|\Psi_{00}|^2$.

(b) $|\Psi_{10}|^2$, 1 node in x-direction

(c) $|\Psi_{01}|^2$, 1 node in y-direction

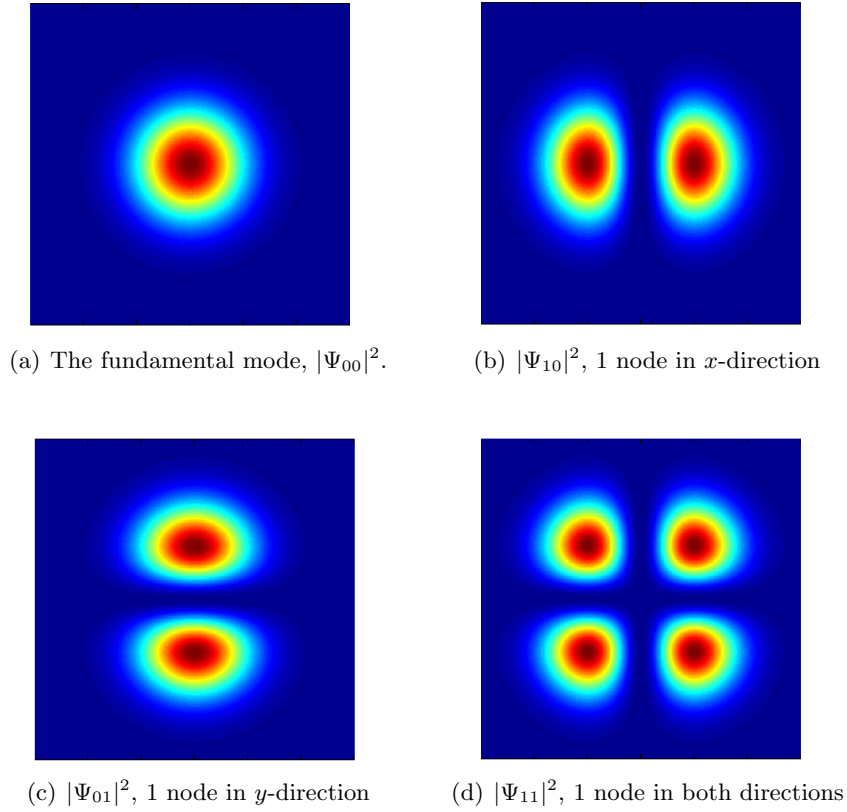(d) $|\Psi_{11}|^2$, 1 node in both directions

Figure 2.5: Plots of a few of the modes predicted by equation 2.1, with $\omega_x = \omega_y = \sqrt{2}$. The indices label the number of nodes, and in which direction they occur. Other higher order modes are easily visualized in the same manner, although the observed modes start deviating towards Laguerre Gaussians.

2.2.2 Complete sample

The sample does not consist of a single cavity, but rather has a 2D array (6×7) of cavities. The individual cavities are indicated by their row and column indices. This means the cavity in the lower left is **R1C1** and the upper right would be **R6C7**. Although slightly confusing, the two samples used for the measurements are indicated by C1 and C2 respectively. Both samples are mounted on the same chip carrier, but have separate electrical connections (sharing the same ground). This means that voltages can only be applied across the entire sample, and not across single cavities. Potentially, having too large currents (on the order of 100–200μA) can cause degradation of the sample over time (see section 3.8 on sample degradation).
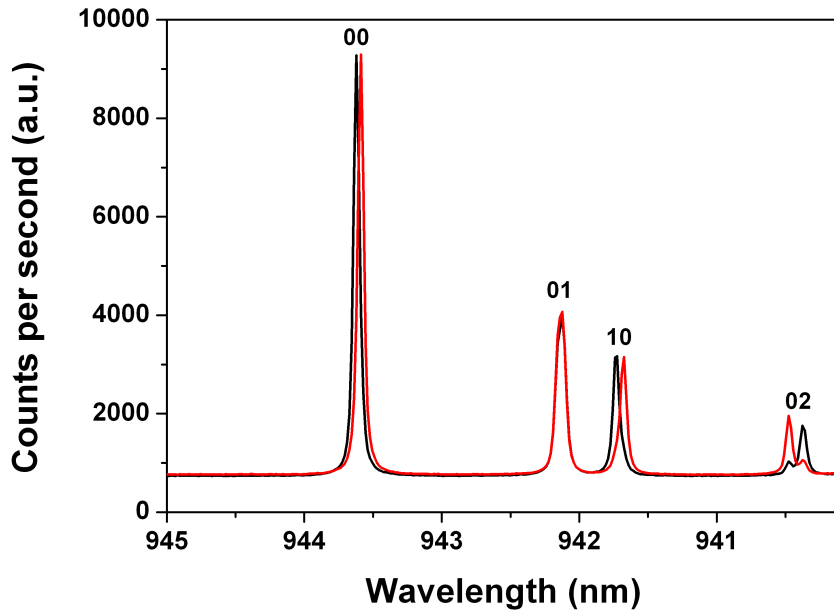
Figure 2.6: An example spectrum of a cavity. The modes are indicated with labels n and m, refering to equation 2.2. The black and red curves are for two orthogonal polarizations. Notice that for the fundamental mode the two polarizations do not overlap, and so this cavity is not (yet) polarization degenerate (but very close to it).

2.3 Methods

Multiple different measurements can be done on the cavities to characterize their properties. After the characterization has taken place, suitable and/or promising cavities can be chosen with which to continue. Continuing in this case means burning holes to get the fundamental mode (FM) to be polarization degenerate. The three useful measurements for characterizing discussed here are the **spectrum** of the cavity, a **voltage** scan and a **spatial** scan.

2.3.1 FM Splitting from photoluminescence

The splitting of the fundamental mode can usually be obtained directly from the spectrum, since generally the initial splitting is large enough to be resolved. The initial splitting of the fundamental mode depends on the geometry and orientation of the trenches, as well as on the resulting size of the oxide aperture. Decreasing the aperture opening (letting the oxide grow in further) generally increases the splitting. A typical value for the initial splitting of the cavities is around 30GHz. Such a splitting can usually be reduced to values close to degeneracy by burning 4–6 holes.

27

2.3.2 Voltage scan

The voltage scans provide a quick overview of the spectral position of the dots. The measurement is based on two separate effects

- Charging of the dots by applying a bias voltage (see section 1.3.3).

- Quantum confined stark effect (QCSE), effectively tuning the dot emission frequency by shifting the energy levels.

By obtaining a spectrum at various voltages, it is possible to track the frequency shifting of the peaks with voltage. A nice way to graphically display this tuning is by creating a 2D plot of the spectrum intensity, with wavelength on the vertical axis and voltage on the horizontal. Such a typical voltage scan is reproduced in Figure 2.7.

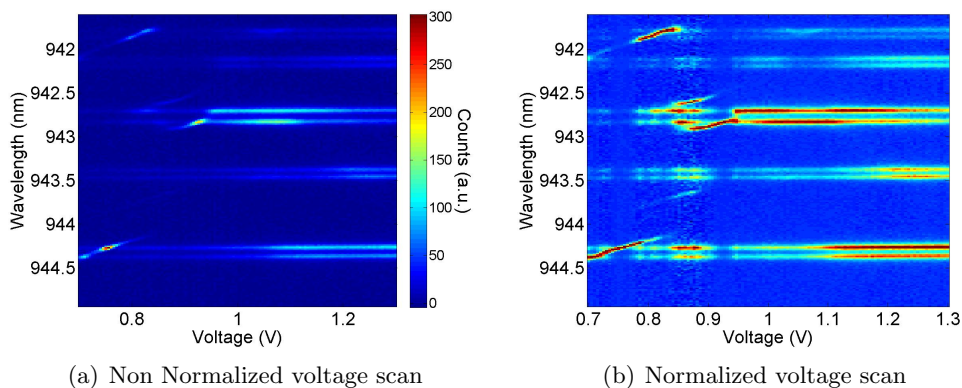(a) Non Normalized voltage scan   (b) Normalized voltage scan

Figure 2.7: Typical voltage scan. The curved lines are characteristic for quantum dots, and should be parabolic. The more or less constant horizontal lines are the cavity modes (the FM being at the bottom).

Notice that some of the peaks spectrally shift as a function of voltage, while others do not. The lines that are more or less constant with voltage are the cavity modes. The cavity modes *do* tune with voltage however (as is discussed in section 3.4), but the effect is too small to be seen using the voltage scans. The quantum dot emission tunes with voltage, and so the sloped curves are quantum dots. It is important to note here that a low pumping power (microwatts) is required to see the dots. Higher pumping power would overpump the dots and only show the photoluminescence of the cavity modes (see section 1.3.5). The laser power is not varied to achieve this low power, but instead neutral density filters are used to attenuate the excitation source.

The voltage scan images are a suitable tool for obtaining information about the spectral position of the dots. Using them, selecting promising cavities based on dots (spectrally) close to the fundamental mode is possible. Apart from that, the voltage scan takes only a few minutes to complete, allowing for a quick characterization.

Notice also that the same QCSE can be used to tune the dots into the fundamental mode by applying a voltage. If the dots are (spectrally) too far away to be tuned into the fundamental mode by applying a bias voltage, it is still possible to coarsly tune them by using the hole burning technique (see section 3.5).

During the measurements it is a good idea to monitor the sample degradation, by recording an IV-curve (see section 3.8). The voltage scans therefore also record the IV-curve.

2.3.3 Spatial scan

One final important parameter is the spatial separation of the quantum dot and the fundamental mode center. The spatial scans provide the information about this distance.

For the spatial scans the PI-stage is used to move the objective across an area of about $10 \times 10\mu$m or $15 \times 15\mu$m, in steps of either 0.5μm or 0.25μm depending on the required resolution. The time it takes for a spatial scan to finish is between half an hour and three hours (depending, again, on the resolution as well as the scanned area).

At each position of the PI-stage, the sample is pumped above bandgap and the *emission* is recorded (so it is the pump that is being scanned). A single mode fiber of 5μm core diameter is used to send the laserlight into the optical setup. The setup has an effective demagnification of $5\times$, and so the sample is scanned using a 1μm spot. At each position of the PI-stage, it is recorded for each frequency wether or not there is emission at that location. Once all the data is obtained, an array of images is made of which each image represents the entire area at a single frequency. In other words, these images are made by putting together the pixels at the same frequency.

Since we know from the stark shift scans at which frequencies the fundamental mode and dot are, we can look at the images for these frequencies and locate their centers. An example of a spatial scan image is given in Figure 2.8.
If the quantum dot is not on resonance with the fundamental mode they do not show up on the same image. If however the dot is on resonance with the fundamental mode, the image at the resonance frequency shows both the fundamental mode and the dot. This is because it is the emission that is being recorded. To find the distance between the dot and the mode, a script was written to fit Gaussian profiles through the images. The centers of these Gaussian curves can then be used to compute the distance.

2.3.4 Hole burning

The hole burning technique is used to tune the polarization degeneracy of a cavity. Since this degeneracy arises mainly because of strain in the material, inducing or releasing extra strain can be a way to tune the degeneracy. The underlying effect of the polarization
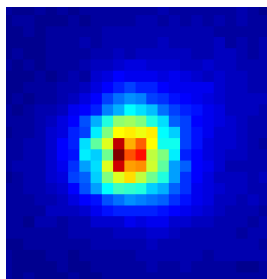
Figure 2.8: An example spatial scan, showing the emission from the fundamental mode. The image is $15 \times 15 \mu m$. A similar image would be obtained for a quantum dot (at a different frequency, and a smaller emission spot).

indegeneracy due to strain is birefringence. Birefringence is the phenomenon that the different polarization directions of light in a material experience a different refractive index. If, for example, a circularly polarized lightbeam enters a birefringent crystal, the two components of the polarization will emerge at the other end having obtained a phase differnce due to differing optical path lenghts. If this phase difference is just right, the beam will now emerge as a linearly polarized lightbeam. This is in effect exactly the principle of a quarter lambda wave plate.

If, instead of exiting the crystal at the other end, the beams are reflected like in a cavity, (constructive) interference causes the two polarization modes to obtain a different frequency. Denoting the two different refractive indices n_1 and n_2, the condition for constructive interference (not including phase shifts) is:

$$2Ln_1 = m\lambda \tag{2.3}$$

stating that the path length ($2Ln_1$) should be an integer multiple (m) of the wavelength λ. The same condition holds for the polarization experiencing the refractive index n_2. For both polarizations L is the cavity length (having a fixed value), and since m is an integer, the wavelength λ has to differ for different refractive indices.

By using an intense laser beam to create small defects on the cavity surface, it is possible to tune this birefringent property. The intense laser beam causes thermal expansion at the surface, which imposes a force (stress) on the sample. It is this stress that deformes the lattice, resulting in strain. Finally, it is this (anisotropic) strain that causes birefringence. A microscope image of a cavity on which holes were burnt is shown in Figure 2.9.
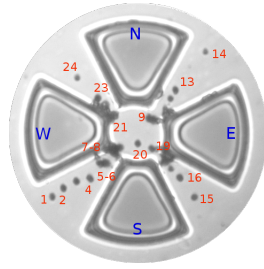
Figure 2.9: A microscope image of a cavity on which holes have been burnt.

It is of course important at what position to burn these defects (and for which duration), in order to decrease (instead of increase) the polarization splitting. A simple but quite accurate model for the hole burning has been described in [5]. Using this model, different computer simulations showed that the right tactic for getting cavities degenerate is by continuously burning the holes at 45 degree angles with respect to each other and the cavity center. Moreover, the two orthogonally polarized peaks do not respond identically to the surface defects. At room temperature, one of the two peaks moves about 4 times as much as the other depending on the location of the hole (also described in [5]).

Chapter 3

Results & Discussion

The most important results and achievements are discussed in this chapter. After discussing the size of the fundamental mode and the characterization of a sample, a complete example on how to obtain polarization degenerate cavities is presented. That section relies on the previously described 'toolbox' of measurement techniques. Finally, some separate but nontheless useful characterization measurements are presented and discussed.

3.1   Fundamental mode waist

The width of the fundamental mode is of importance for the coupling efficiency. It sets the scale for the distance from the mode center at which a quantum dot is still able to couple to the fundamental mode.

As already stated in equation 2.2, the spectrum of the cavities follows the formula

$$\lambda_{\mathrm{nm}} = \lambda_{00} - an - bm$$

By looking at the difference in wavelength between the fundamental mode λ_{00} and the first two higher order modes λ_{10} and λ_{01}, values for a and b can be obtained through[1]:

$$a = \lambda_{00} - \lambda_{10} \quad \text{and} \quad b = \lambda_{00} - \lambda_{01}$$

Further theoretical analysis (see for example [10]) shows that

$$a = \frac{2n_0}{\pi}\left(\frac{h}{l}\right)^2 \frac{1}{r_x} \quad \text{and} \quad b = \frac{2n_0}{\pi}\left(\frac{h}{l}\right)^2 \frac{1}{r_y}$$

$$\lambda_{00} = 2n_0\left(\frac{h}{l}\right) - \left(\frac{a+b}{2}\right)$$

---

[1]Ideally, all of the modes would be polarization degenerate. Since this is not the case, values for a and b are obtained for both polarizations separately, and the final result is an average over the two.

Using the latter of these it is possible to find the ratio h/l, in which h is an effective (spatial) separation between the electric field nodes in the z-direction, and l labels the different modes in this direction. From the value of h/l and the values of a and b, the values for r_x and r_y can be obtained. These parameters are related to ω_x and ω_y in equation 2.1 for the cavity modes through

$$\omega_{\mathrm{x,y}} = \sqrt{\frac{\lambda\, r_{\mathrm{x,y}}}{\pi}}$$

Finally, a measure for the size of the fundamental mode is the FWHM of the Gaussian shape. Since the observed pattern is the square of the given equation (introducing a factor 2 into the exponent), the final result is

$$\mathrm{FWHM}_{\mathrm{x,y}} = \sqrt{2\ln(2)}\,\omega_{\mathrm{x,y}}$$

The values for the width of the modes in both directions is on average in the range of 3–4 **microns**.

3.2   Sample characterization

The characterization of the sample is useful in selecting promising cavities to be used for further experiments. The best cavities have a dot spectrally close to the fundamental mode, and already have a small splitting. The first steps in characterization do not involve spatial scans simply because they take 1–3 hours to complete (depending on the resolution). This means that for each cavity the following two steps are taken:

1. Align on cavity, and obtain its spectrum. From this spectrum, the splitting can be extracted using one or multiple fits. This procedure is described in some more detail in section 3.3.1).

2. Perform a voltage scan, to see the spectral position of the dots.

Table 3.1 shows the initial splittings (in GHz) of sample C2. Some of the cavities were not scanned since their fundamental mode was at too low a frequency (out of range for the pump laser).

To point out that the splitting is not enough to characterize the cavities, Figure 3.1 shows the voltage scans for R5C2 and R4C6. R5C2 seems to be a good candidate because of its splitting, whereas R4C6 has a larger than average splitting. The voltage scans show however that R4C6 has a quantum dot nicely tuning into the fundamental mode, and might therefore actually be the best choice. As a general remark, before starting the voltage scans it was first checked if any dots were visible at all using the spectrometer.

	C1	C2	C3	C4	C5	C6	C7
R1	41.86	36.38	23.43	20.73	25.67	–	–
R2	31.40	23.90	18.24	18.41	29.70	–	–
R3	19.67	13.51	14.59	15.60	34.53	–	–
R4	11.80	12.31	18.77	18.99	30.80	39.82	50.72
R5	13.64	10.64	15.48	21.17	33.12	–	55.71
R6	10.24	16.43	16.63	31.61	28.96	–	58.19

Table 3.1: Table of initial splittings (in GHz) of sample C2. Some cavities were not scanned because their fundamental mode wavelength was out of the Velocity tuning range (which would exclude reflection measurements).

(a) R5C2   (b) R4C6
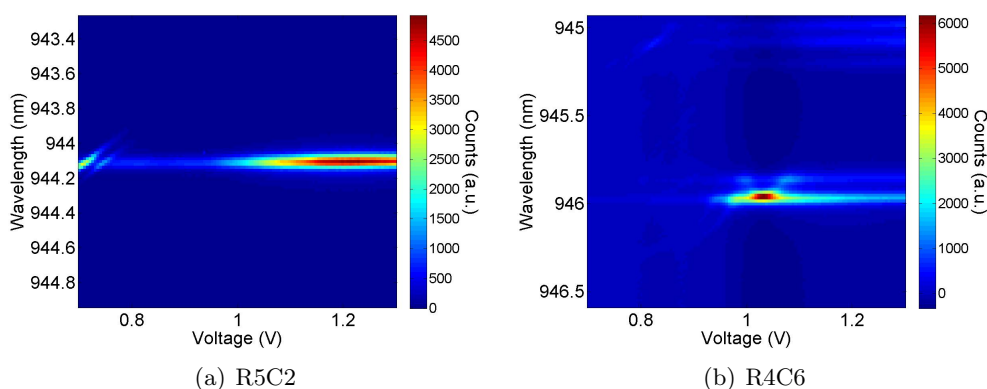
Figure 3.1: (a) Voltage scan for R5C2 (b) Voltage scan for R4C6. Even though R5C2 has the best value for the initial splitting, R4C6 is the more promising candidate.

3.3 Getting a cavity degenerate

This section describes all of the necessary steps to fully characterize a cavity (and hence sample), and to make the fundamental mode polarization degenerate, using the methods described in Chapter 2. It is assumed here that the 780nm (above bandgap) diode laser is aligned on the cavity that is to be characterized. In the next few subsections, the complete procedure and results will be discussed using cavity R2C5 (on sample C1) as an example.

3.3.1 Spectrum

Once the laser is aligned, the spectrometer shows the mode spectrum of the cavity. The spectrum for R2C5 looks like as shown in Figure 3.2. If the splitting is larger than the resolution of the spectrometer (0.01664nm), two split peaks can easily be distinguished on the fundamental mode. A note to be made is that the spectrometer spectra are plotted versus pixel numbers. These pixel numbers are related to the wavelength λ in

nm via (obtained using a calibration lamp):

$$\lambda = \lambda_\text{s}\text{nm} - 0.01664 \cdot \text{pixel} \qquad (3.1)$$

where λ_s is the wavelength at which the spectrometer is centered.
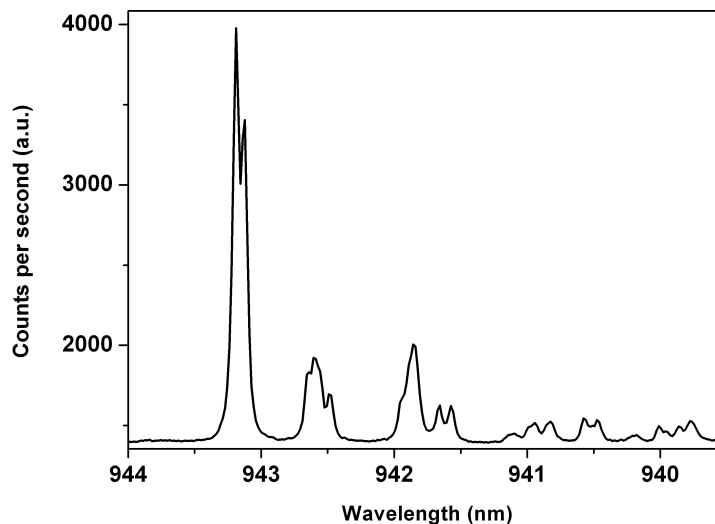

Figure 3.2: The cavity spectrum of R2C5. The fundamental mode (highest wavelength) has a splitting larger than the resolution of the spectrometer, and can therefore be seen as 'split'. For a polarization degenerate cavity, the splitting is no longer observable on the spectrometer. Because of overpumping, the quantum dots are not visible in this spectrum.

For a quantitative splitting value however, the spectrum should be saved and fitted. To slightly make the fitting more easy, it is also possible to insert a polarizer and half-lambda plate in front of the spectrometer, so that it is possible to 'select' either of the peaks and save them separately. Using for example Origin or Maple, a Lorentzian can be fit to the data and the peak separation can be extracted. The initial splitting of this cavity, obtained from the fits shown in Figure 3.3, is 0.038 nm (or 12.56 GHz).

3.3.2   Voltage scans & Hole burning

Since the cavity is not polarization degenerate, the hole burning technique can be used to decrease the splitting. It is also important to find out if there are any potentially good quantum dots in the vicinity (spectrally) of the fundamental mode. To obtain information about the latter, a stark shift can be used. The stark shift scan of R2C5 before burning any holes is shown in Figure 3.4.
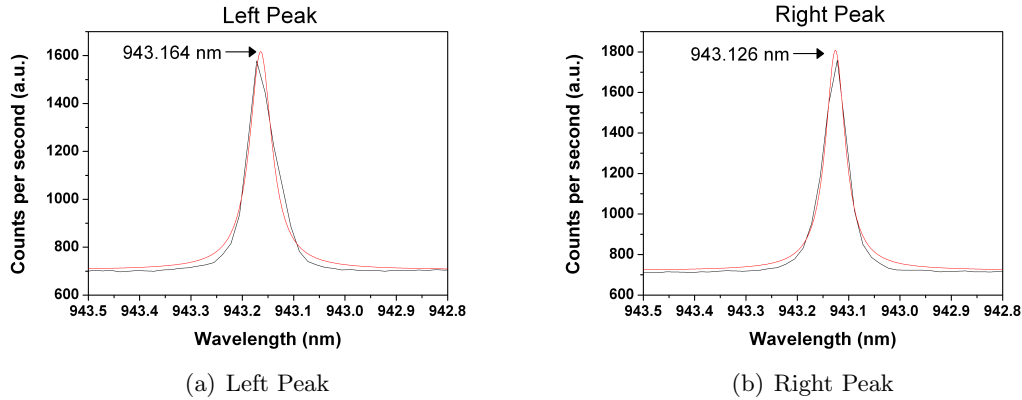
(a) Left Peak
(b) Right Peak

Figure 3.3: Lorentzian fits of the two peaks of the fundamental mode. The separate peaks were obtained using a polarizer and half-lambda plate in the output collection. The left peak is shown in (a), and the right peak is shown in (b). The value of the splitting is the (absolute) difference of the centers of the peaks, and equals 0.038 nm in this case.
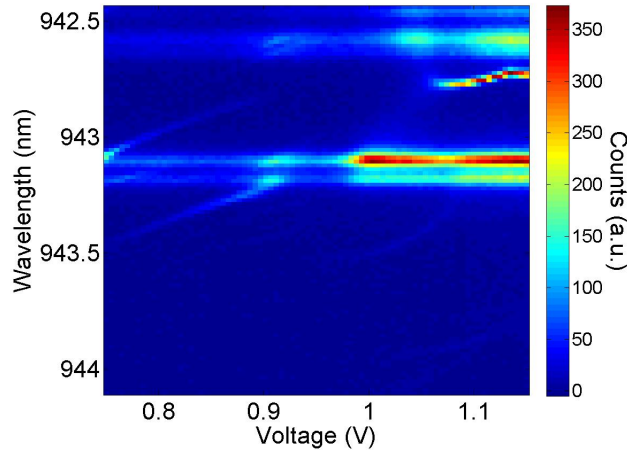

Figure 3.4: The stark shift scan of R2C5 before burning holes. The splitting of the fundamental mode is easily visible, and there are potential dots tuning into the fundamental mode.

The next step is to burn holes to get the cavity polarization degenerate. The results for the first few holes are summarized in Figure 3.5.

The cavity splitting is at this point no longer distinguishable using the stark shift (or spectrometer). To obtain the actual splitting, reflection measurements have to be used (see section 3.3.3). Notice also that the absolute wavelength of the fundamental mode has shifted. More strikingly is that it is obvious that the quantum dot emission gets redshifted, and that the effect of hole burning is larger on the dots than on the

36

(a) 1 hole

(b) 2 holes

(c) 3 holes

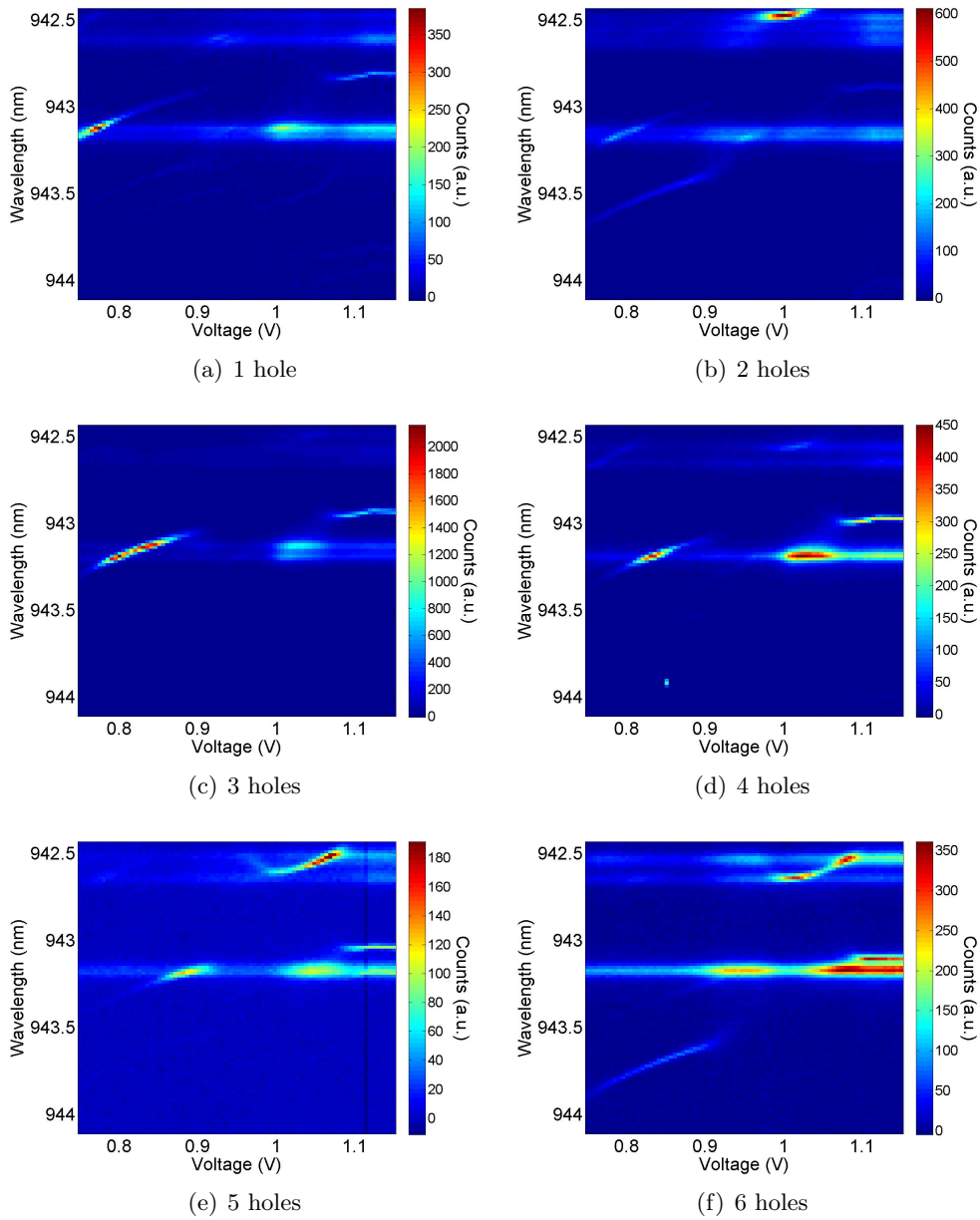(d) 4 holes

(e) 5 holes

(f) 6 holes

Figure 3.5: The results of the first few holes burnt on R2C5. The splitting of the fundamental mode decreases to a point where it is no longer visible using the spectrometer (and hence not on the stark shifts). The splitting has to be obtained from reflection measurements. It is not only the cavity modes that are affected by the hole burning. It is clearly visible that the quantum dot emission also shifts to higher wavelengths.

modes. This can either be a problem or be very helpful. The fact that the quantum dot emission shifts might be used in a controlled way to tune quantum dots into resonance

37

with the fundamental mode by burning holes. This would mean that holes have to be burned isotropically, in such a way that the splitting of the fundamental mode is not changed. Because the effect on the dots is larger, the dots effectively move with respect to the modes. Inducing strain isotropically has been tried, and the result is summarized in Figure 3.6.
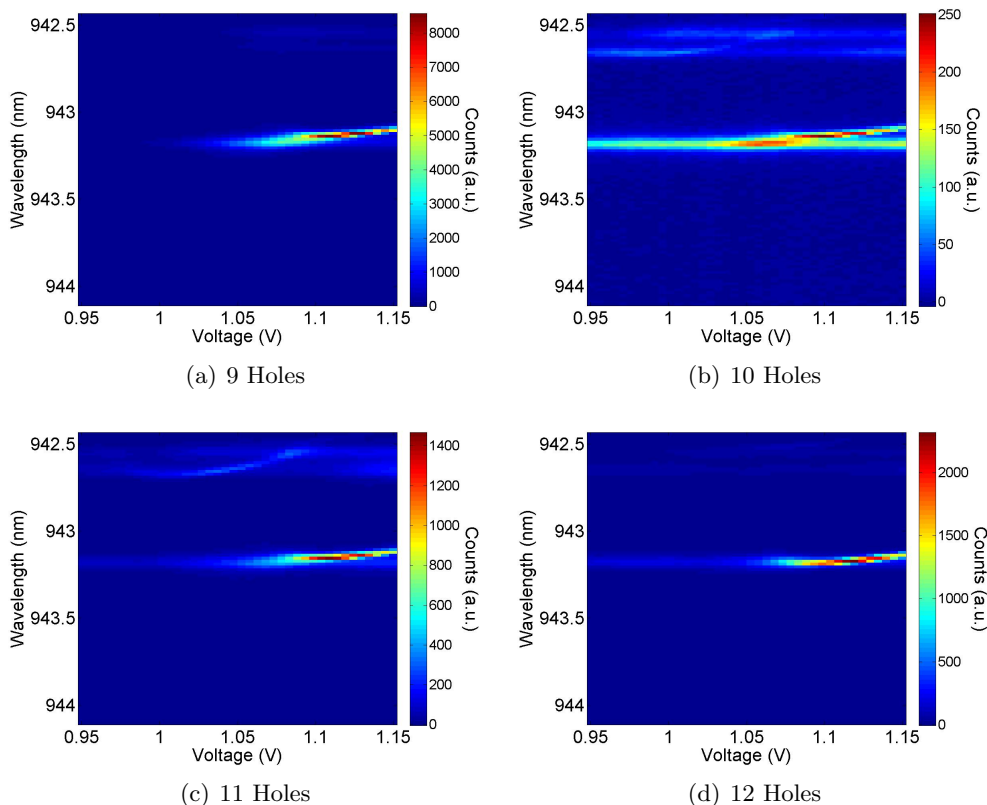

(a) 9 Holes

(b) 10 Holes

(c) 11 Holes

(d) 12 Holes

Figure 3.6: The results of isotropically burning holes on R2C5. The splitting of the fundamental mode is unchanged, while the quantum dots cleary shift in wavelength. This effect can be used to control the quantum dot emission frequency. The voltage range has been adjusted w.r.t. Figure 3.5.

This shifting of the quantum dot emission is further discussed in section 3.5. It is necessary to clarify the isotropic strain. As discussed in section 2.3.4, burning holes moves the separate peaks by different amounts based on the location of the hole. By burning two successive holes at orthogonal positions, a net movement of the peaks is achieved without changing the peak separation. This is what is meant by isotropic strain.

3.3.3 Reflection Measurements

At this point, R2C5 is seems to be a degenerate cavity with a quantum dot tuned into resonance at about 1.13 V. This is the perfect situation for reflection measurements,

which provide data about the actual splitting of the fundamental mode as well. The reflection dips of the two peaks are shown in Figure 3.7.
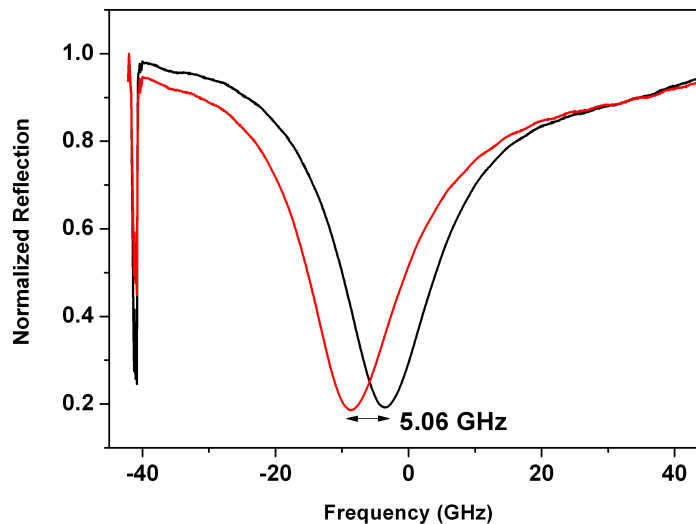

Figure 3.7: The two reflection dips of R2C5. Their separation is about 5 GHz, which is equivalent to about 0.009 nm. In other words, this splitting is no longer visible on the spectrometer (which is what the starkshift shows). On the other hand, the cavity is not yet sufficiently degenerate ($\sim 2\,GHz$). The frequency axis is with respect to the laser frequency (which is unimportant for the value of the splitting). The spikes on the left hand side are laser artifacts.

Since a good enhancement of the dot emission with respect to the cavity mode is observed (see Figure 3.6(d)), a good reflection peak is also expected. The actual peak, however, is shown in Figure 3.8.

As can be seen, the peak height is very small. A possible explanation might be the spatial position (discussed in the next section) of the dot with respect to the fundamental mode. The larger the distance between the quantum dot and the fundamental mode, the smaller the coupling.

The record degeneracy achieved through hole burning is 0.2GHz, starting with a cavity that had an initial 50GHz splitting (see Figure 3.9). To reach this degeneracy, 27 holes were burnt (the average number of holes needed has been reduced to 4–5 holes).
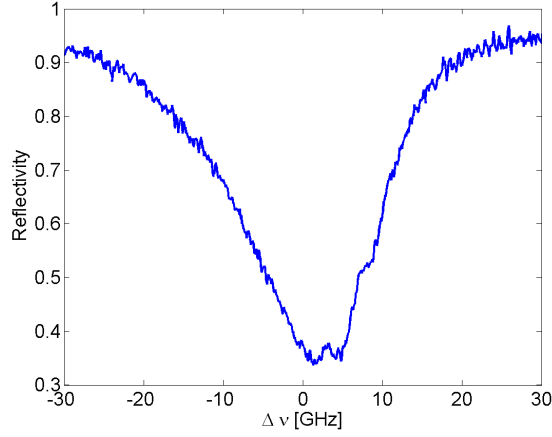
Figure 3.8: Reflection measurement on degenerate cavity R2C5 with quantum dot tuning into resonance. The peak height is (very) small, which might be explained by the fact that the dot is spatially not nicely centered on the fundamental mode center.

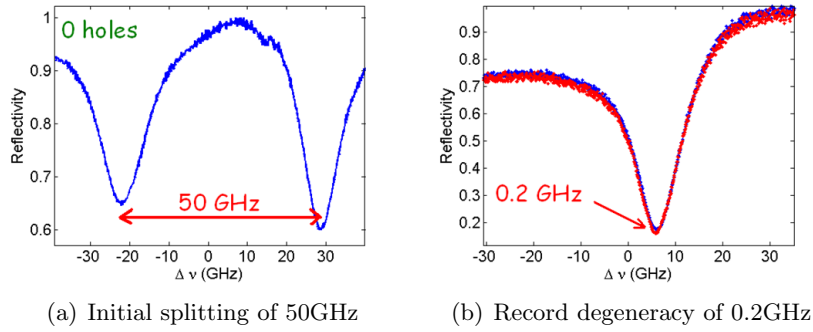(a) Initial splitting of 50GHz

(b) Record degeneracy of 0.2GHz

Figure 3.9: (a) The initial splitting of the cavity was roughly 50GHz. (b) By burning 27 holes on the cavity, the degeneracy was reduced to a record value of 0.2GHz.

3.3.4   Spatial Scan

A spatial scan has been performed on this cavity to find the position of the dot and of the fundamental mode. The distance between them can then be extracted from this data. From the last stark shift (Figure 3.6(d)) it is known at what wavelength the fundamental mode and dot are visible. It can also be seen that at about 1.15V the dot is out of the fundamental mode, while both should still be visible. The scan was performed at a slightly higher voltage (1.204V), since at this voltage the result was even more clear. The scan should show the fundamental mode and the dot at their corresponding frequencies. These images are shown in Figure 3.10.

The extracted distance between the quantum dot and the fundamental mode is 4.3μm,
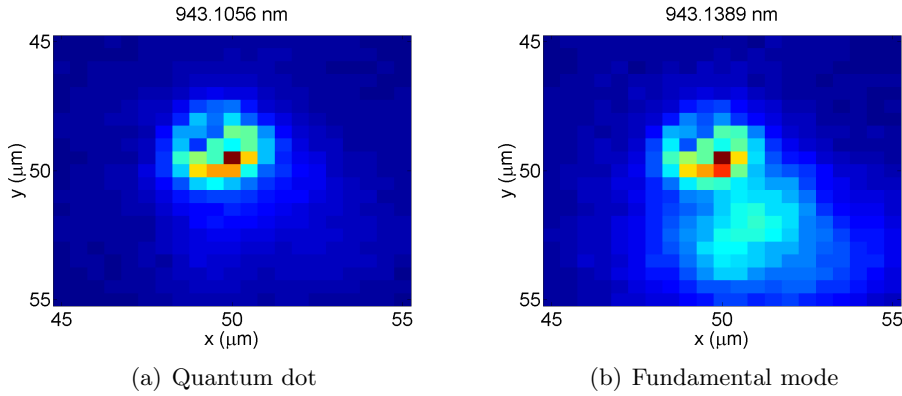
40

(a) Quantum dot   (b) Fundamental mode

Figure 3.10: The results of the spatial scan at 1.204 V on R2C5. This voltage is not present in the starkshift image, but the position of the fundamental mode and dot can still be seen on the spectrometer. Part (a) shows the quantum dot, and (b) shows the fundamental mode (the quantum dot is still visible, since it is still coupled to the fundamental mode). The distance between the dot and fundamental mode is 4.3μm, probably explaining the low reflection peak.

and was obtained by fitting Gaussian curves through both images. This procedure works as follows:

- If possible, the indices of the pixel with the highest intensity are taken from the image. In the above two images, this is clearly possible for the quantum dot. For the fundamental mode, a different wavelenth than shown was used in which the relative intensity of the fundamental mode was higher than the quantum dot.

- A Gaussian curve is fit through bot the column and row indicated by the indices of the pixel. The centers of these fits can then be used to compute the distance between the dot and the fundamental mode. Denoting the coordinates of the dot and fundamental mode by (x_{qd}, y_{qd}) and (x_{fm}, y_{fm}) respectively, the spatial separation D is simply found by using the pythagorean theorem:

$$D = \sqrt{(x_{qd} - x_{fm})^2 + (y_{qd} - y_{fm})^2}$$

By taking a characteristic fundamental mode width w of about 3μm, the Gaussian shape of the mode makes it such that at the abovementioned distance d of 4.3μm the coupling efficiency g is on the order of 10 percent of the maximum g_0:

$$g(d) = g_0 e^{d^2/w^2} \quad \Rightarrow \quad g(4.3)/g_0 = e^{4.3^2/3^2} \approx 0.13$$

If the quantum dot would have been within a 1μm radius, the coulping would be closer to 75%.

3.4 Voltage-tuning of the cavity modes

The reflection measurements provide us with quantitave data about the voltage dependence of the cavity modes. In general the effect of changing the birefringence by applying an electric field is either called the **Pockels** effect or the **Kerr** effect, depending on wether the effect is linearly or quadratically proportional to the applied field respectively. The voltage-tuning in this experiment was observed to be in the linear regime. The frequencies of the two orthogonally polarized peaks of the fundamental mode have been tracked, and are observed move with about 5 GHz and 3 GHz per volt. This result is shown in Figure 3.11. It can be seen that the effect is not the same for different polarizations, which is due to a differing effect of the electric field on the refractive indices.
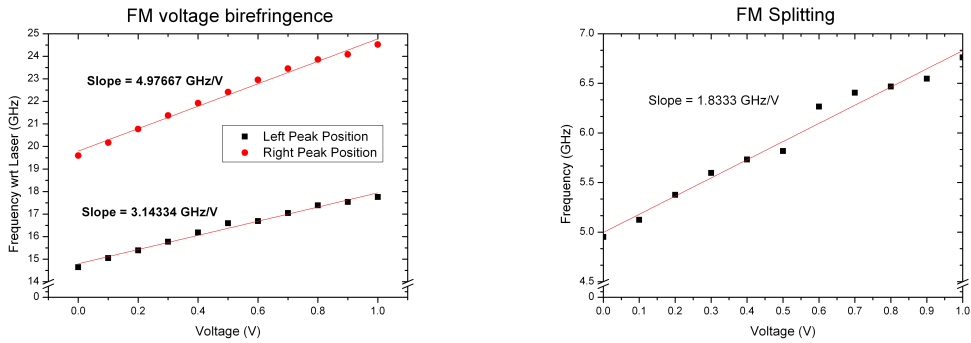
(a) Frequencies (wrt laser) of individual peaks   (b) The frequency difference (i.e. splitting)

Figure 3.11: (a) Shifting of the two fundamental mode peaks by applying a voltage. The peaks move differently due to anisotropic interactions of the semiconductor atoms (birefringence). (b) The splitting of the two peaks as a function of voltage. The splitting is just the difference in frequency of the peaks.

3.5 Strain-induced quantum dot spectral shifting

The shifting of the dots has been analyzed for multiple cavities. In all cases, the shifting seems to have a preference in the direction towards higher wavelengths. This conclusion is made based on the graph shown in Figure 3.12. Multiple of such graphs have been made, all with the same results.

There is no solid understanding of this preference for redshifting. This effect is known also in literature [6], [13], [19]. A model is expected to be developed in the near future.

3.6 Reflection peak nonlinearity

The height of the peak in the dip is predicted to decrease nonlinearly with increasing pump-power [2], [21]. The effect has already been seen in another experiment [8]. The
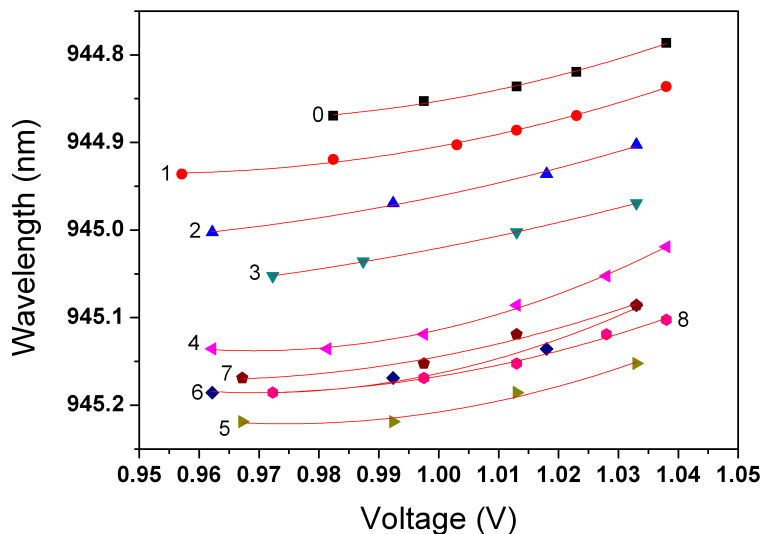
Figure 3.12: Tracking of the shifting of the dot emission. The numbers label the holes. Clearly, there is a tendency for the emission wavelength to redshift. Two holes (numbers 6 and 7) apparently blueshifted the emission, while hole 8 caused a redshift again. There is as of yet no theory for the direction of the shift.

reason for the nonlinearity is because of saturation of the quantum dot at very low intensities (on the order of 1 photon per lifetime). Intuitively, this can be visualized by considering a few photons heading towards the cavity. The first photon gets absorbed and raises the system into the excited state. For as long as the system remains excited (i.e. the systems lifetime), any other photon is unable to act since there is no state to be excited. Hence for all the other photons, the cavity is effectively transparent. This mechanism is graphically shown in Figure 3.13.

Increasing the power of the pumping laser, more photons see an effectively empty cavity. Since we are in effect are temporaly averaging using the photodiodes, the result is that the average peak height decreases (becomes more transparent). This effect has been measured by pumping the sample with different OD filters, instead of direcly varying the laser power. The power then follows the relation

$$P = P_0 \times 10^{-\text{OD}}$$

in which P_0 is the output power of the laser, which can be measured simply using a powermeter (750μW in this case). By varying the OD filters, different powers are send onto the sample. In principle then, any power $P \leq P_0$ can be obtained for a given P_0 by changing the OD value. In practice however, a limited set of OD filters is available. The available OD values in this case were x, x.3 and x.5, in which x is either 6, 7, 8 or

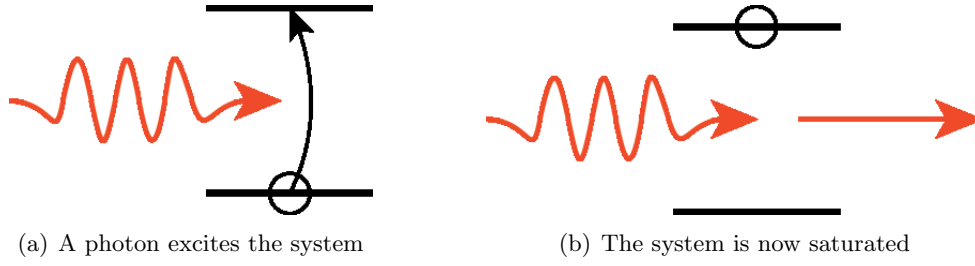(a) A photon excites the system   (b) The system is now saturated

Figure 3.13: (a) A photon gets absorbed excites the system. (b) The system is now saturated, since other photons reaching the system can not excite it anymore. Hence for as long as the system remains in the excited state (lifetime), the cavity is effectively transparent.

9. In order to get different powers (for more data points), the laser output power P_0 was altered to 430μW once. For this new laser power P_0', the same range of OD filters was used again. The effective OD at the previous P_0 can then be recalculated via

$$\text{OD} = \log\left(\frac{P_0}{P_0'}\right) + \text{OD'}$$

The height of the peaks is extracted by fitting the reflection measurement data. The function to fit the reflection dip and peak is given by (see [2])

$$R(\omega) = \left|1 - \frac{\kappa(\gamma - i(\omega - \omega_{QD}))}{(\gamma - i(\omega - \omega_{QD}))(\kappa - i(\omega - \omega_C)) + g^2}\right|^2 \tag{3.2}$$

where the parameters κ, γ and g are as discussed in section 1.4 and where ω_{QD} and ω_C are the resonance frequencies of the quantum dot and cavity respectively. Since there is no spin-pumping in this case, the fits were made by averaging over a coupled ($g \neq 0$) and non-coupled ($g = 0$) case:

$$\texttt{Fit} = \frac{R(\omega, g \neq 0) + R(\omega, g = 0)}{2} + \text{offset}$$

The heights of the peaks are then taken with respect to the offset, which represents the value at which the reflection dip would have been without a dot on resonance. Examples of relfection peaks and fits are shown below in Figure 3.14.

To compare with the theory, Figure 3.15 shows the peak height as a function of power. It also shows the fit of the function as found in [2], restated here as

$$V(P) = \frac{V_0}{(1 + P/P_c)^2}$$

in which $V(P)$ is the visibility as a function of power P, and P_c is the so called critial power at which the visibility is reduced to 25%.
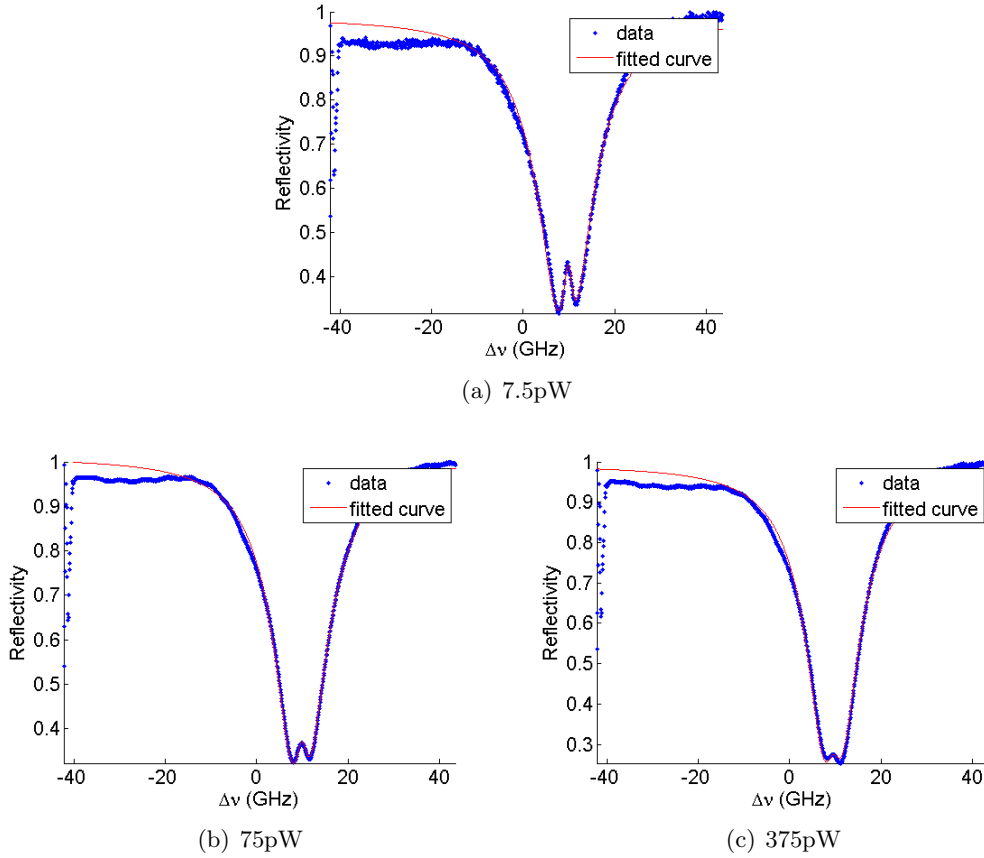
44

Figure 3.14: The data and fits of the reflection peaks at various powers (using different OD filters) (a) Reflection peak at OD8 ∼ 7.5pW. (b) Reflection peak at OD7 ∼ 75pW. (c) Reflection peak at OD6.3 ∼ 375pW.

The values obtained are $V_0 = 0.134$ and $P_c = 271$pW. A power of 271pW corresponds to about 1.27×10^9 photons per second reaching the cavity. Since the lifetime of the cavities is about 100–200 picoseconds, this means an average of about one fifth to a quarter of a photon reaches the cavity per cavity lifetime. This observation matches the theoretically exact value of one quarter photon per lifetime.

3.7   Polarization measurements on reflection peak

By inserting a polarizer in the collection path, the different polarizations can be analyzed. Since the two reflection dips are orthogonally polarized, they can be observed separately. A fit of the reflection dip center for different polarizer angles is shown in Figure 3.16. The peak-to-peak separation of the graph is equivalent to the frequency splitting (0.126 GHz) between the two peaks. This splitting is surely in the degenerate range.
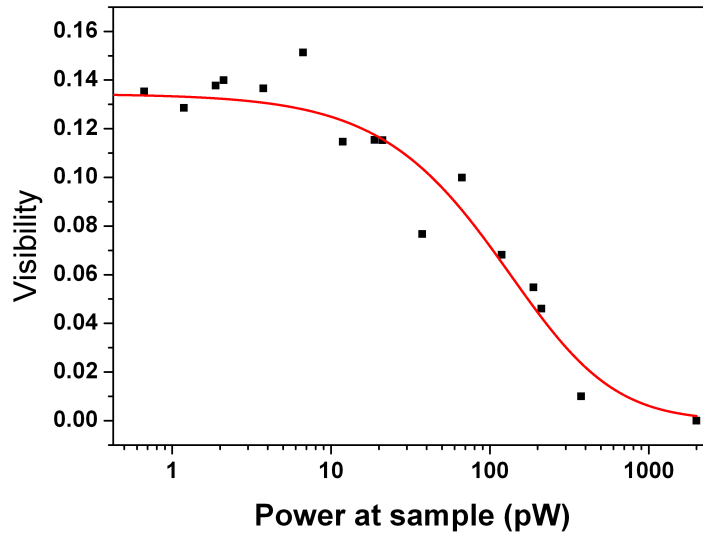
Figure 3.15: The power dependence of the peak height. The fit is to compare with the theoretical predictions of [2]. The critial power parameter P_c extracted from the fit is 271pW.

3.8 Degradation

It was found that the samples are degrading over time. The are several possible reasons or triggers for this degradation. The most obvious are the hole burning and the effects of applying voltages and currents to the sample. Effects caused by cooling down and warming up on a daily basis also have to be taken into account.

3.8.1 IV-Curves

As already mentioned, the sample should behave essentialy like a PIN diode as far as its electrical properties go. The IV-curve for a properly working sample hence looks like the one shown in Figure 3.17. These IV-curves were measured during the Stark Shift scans.

Figure 3.18 shows the IV-curves taken at the end of a given day (after burning the eigth hole), and the IV-curve taken first thing next morning before burning holes. As is obvious, the two curves look completely different. Even more imporant though, is that on this next day the sample no longer has a diode-like IV-curve, indicating degradation. It is not known what caused this sudden degradation.

- Hole-burning seems an obvious candidate for causing degradation. The first 5 holes were burnt at half the power (125 mW) as compared to holes 6–8, and the sample
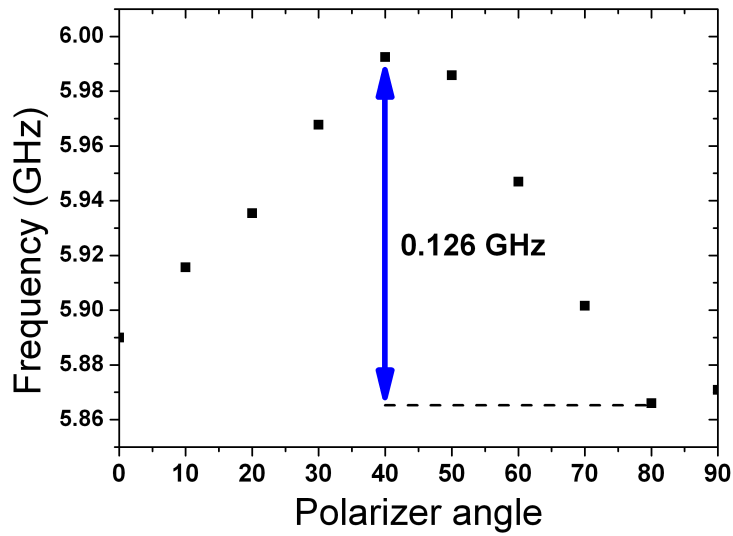
Figure 3.16: Reflection dip center as a function of polarizer angle. The splitting (0.126 GHz) of the two peaks can easily be extracted as the peak-to-peak difference. This cavity is evidently in the degenerate range.
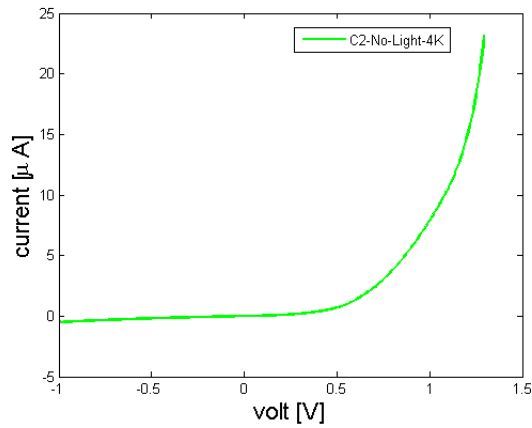

Figure 3.17: The IV-curve as it should look for a correctly functioning sample.

did not show any degradation the next day. The duration for all of the hole burns was roughly 20 seconds.

- Applying a voltage across the sample causes a current through it. This current heats the sample, which might be causing the degradation.
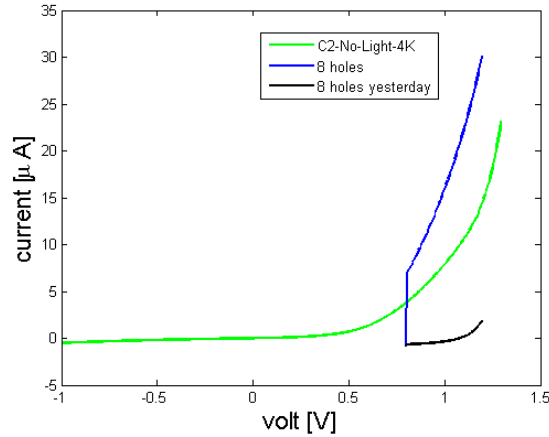
Figure 3.18: The IV-curve for the eigth hole (yesterday) still looks like a normal diode. The IV-curve for the eigth hole on the next day has shifted considerably up in current. This is a sign of degradation, for which there is no solid explanation yet.

Both of the above explanations have in common that they heat the sample, which could be the fundamental reason for the degradation. They do not in themselves explain the 'suddenness' of this degradation from one to the next day. It is important to also take into account the warming-up and cooling-down of the sample from day to day, which can possibly explain the suddenness.

3.8.2 Memory effect

Another effect is seen when monitoring the IV-curves, which has been named a memory effect. By turning on and off the pump laser, carriers are created or not, respectively. It was expected however, that when the pump laser is off, the created carriers would recombine so that when the laser was turned on again, the current in the sample had been reset. This was not the case, as Figure 3.19 shows. A possible explanation is that charges are being trapped or stored, much like as if there was a capacitor present.

3.9 Positioning samples

Since the samples degraded, new samples have to be fabricated. These degraded samples had a high concentration of quantum dots, with a randomly positioned matrix of cavities. Because of the high quantum dot concentration, there was a high chance for most of the cavities to have a dot positioned nicely in the center. For the new samples to be fabricated, a raw sample was available with only quantum dots and no cavities (i.e. only the DBR structures and active layer). Instead of cavities, the sample has several markers (boxes), which serve as a reference point for positioning the cavities. By scanning the
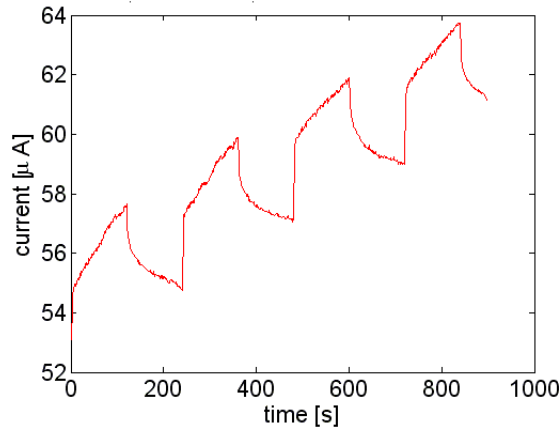
48

Figure 3.19: IV-curve showing the memory effect. Upon turning on the pump laser after it has been off for a while, the current value continues from where it ways. This indicates that charge is somehow being stored, as in a capacitor.

boxes spatially for dots and noting their positions with respect to a specified corner of the markers, the cavities can be accurately positioned such that they have a dot in the center. Of course, for such scans the stability is an important factor (and is described below in section 3.9.2).

3.9.1 Positioning

This subsection describes the procedure for locating a dot and finding its coordinates relative to the markers. Similar positioning has already been done for photonic crystals [26]. In a sense, it is the opposite of the characterisation scans done before. The procedure starts by doing a $10 \times 10 \mu m^2$ spatial scan, combined with a "cross" scan. A cross scan acquires the same data as a spatial scan, but instead of scanning a square area it scans two orthogonal lines each $100 \mu m$ (total PI-stage range). Since the boxes are about $60 \times 60 \mu m^2$, the cross scan data should show the markers (via abscence of the photoluminescence signal). A cross scan is done once before and once after the spatial scan, to obtain information about the stability.

By first plotting the cross scans the same way as is done for the voltage scans, the markers are clearly visible (see Figure 3.20). From these images it is easy to select those spectra at which the markers are most clearly visible (in this case around pixel number 300). This spectrum can then be taken separately, and the exact positions of the markers can be extracted by fitting the dips.

The first thing to note is that the difference in marker positions is more than $60 \mu m$, meaning that the PI-stage movement axes are not aligned along the box markers. On the assumption that the angle between the markers and the PI-stage axis is smaller
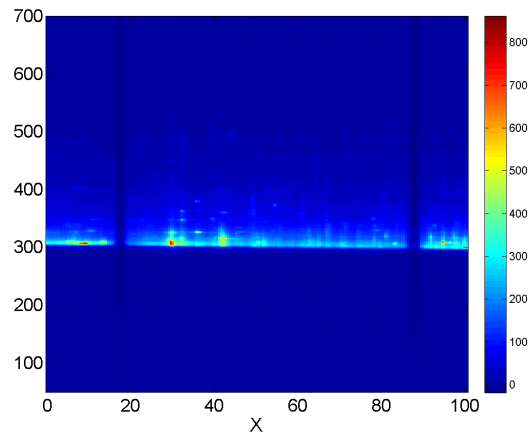
(a) Cross scan voltage plot
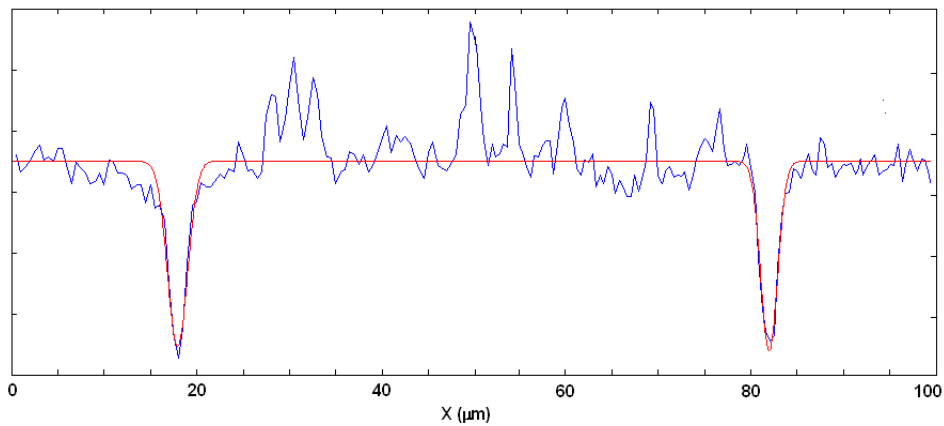
(b) Fit along horizontal line at pixel 300

Figure 3.20: (a) Plot of a cross scan, clearly showing the position of the markers (absence of the photoluminescence signal). At pixel number 300 the spectrum should clearly show a dip at the marker positions (there are of course more frequencies at which the dip is visible, but contrast increases fit accuracy). (b) Fit of the marker dips, this data shows the spectrum along pixel number 300.

than 45 degrees[2], a little algebra is necessary to find the exact angle. Once this angle is obtained, the positions of the quantum dots can be accurately stated with respect to a chosen origin.

---

[2]This is not the full assumption. More precisely stated, the assumption is made that the axes of the PI-stage cross opposite sides of the box marker. If the origin of the PI-stage axes were exactly in the box center, this would be equivalent to a rotation of less than 45 degrees. The previous statement works also for a displaced origin, although the exact maximum angle of course also depends on this position.

Mathematically, the two different frames (the markers and the PI-stage axes) are related through a translation and a rotation. Consider the situation shown schematically in Figure 3.21.
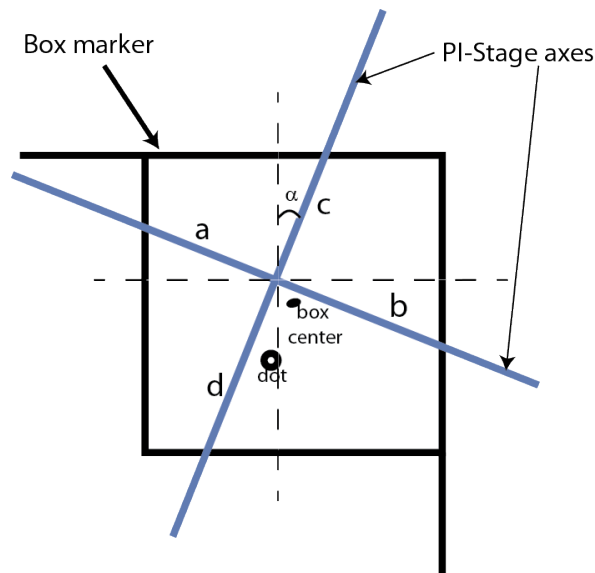

Figure 3.21: Schematic of the situation in the positioning spatial scans. The black lines form the markers (the box), whereas the blue lines denote the orientation of the PI-stage axis. As can be seen, in general the two frames are related through a translation and a rotation. The coordinates of the quantum dots are given with respect to the upper left corner, with x and y increase towards the right and bottom respectively.

Since the boxes are (i.e. should be) $60 \times 60 \mu m^2$, the following condition should be satisfied:

$$(a + b) \cos \alpha = 60$$

from which

$$\alpha = \arccos \left(\frac{60}{a + b} \right)$$

The parameters a and b are the distances extracted from the cross scans, and so this provides a way to find α. The average value found for α is 37.4 ± 0.2 degrees.

Before rough alignment (by eye) of the scanning spot on the center of a box, the PI-stage coordinates are set to $(50, 50)$ (these coordinates are just for reference). Using the spatial scans, the position of several of the brightest dots are noted and a voltage scan is performed at these respective position. The voltage scans can then be compared to select the dot around which the cavity should be positioned.

To calculate the position of the quantum dot with respect to the box markers, its position with respect to the PI-stage axis (from the spatial scans) is noted. The coordinates of the quantum dot with respect to the marker are then found by taking the coordinates of the PI-stage axes origin, and adding the rotated position of the dot with respect to the same PI-stage axes.

$$\begin{pmatrix} x_{\text{dot}} \\ y_{\text{dot}} \end{pmatrix}_{\text{box}} = \begin{pmatrix} x_{\text{origin}} \\ y_{\text{origin}} \end{pmatrix} + \begin{pmatrix} \cos\alpha & -\sin\alpha \\ \sin\alpha & \cos\alpha \end{pmatrix} \begin{pmatrix} x_{\text{dot}} \\ y_{\text{dot}} \end{pmatrix}_{\text{PI}} \tag{3.3}$$

where

$$\begin{pmatrix} x_{\text{origin}} \\ y_{\text{origin}} \end{pmatrix} = \begin{pmatrix} a\cos\alpha \\ b\cos\alpha \end{pmatrix} \quad \text{and} \quad \begin{pmatrix} x_{\text{dot}} \\ y_{\text{dot}} \end{pmatrix}_{\text{PI}} = \begin{pmatrix} x_{\text{dot,PI}} - 50\mu\text{m} \\ y_{\text{dot,PI}} - 50\mu\text{m} \end{pmatrix} \tag{3.4}$$

are the coordinates of the PI-stage w.r.t. the box markers and the coordinates of the dot w.r.t. the PI-stage origin respectively. The calculated positions for the selected dots, including also voltage scans at those positions, are summarized in the accompanying `positions.pdf` file.

3.9.2 Stability

As already mentioned, a cross scan was made before and after the spatial scans to obtain information on the repeatability and stability of the scan. The average fluctuations in these scans was found to be about 0.3 micrometer, which is accurate enough for cavity placement. Another verification for the stability of the scans was done via repeating a spatial scan at the same position. One of the two spatial scans has some artifacts however, as can be seen in Figure 3.22. There are multiple 'jumps' in the middle region of the scan, complicating the comparison of the two scans. Only dots in the upper and lower half have been selected, since these were the largest jump-free regions. The result is summarized in Figure 3.23. It can be concluded from this image that the top and bottom halves are not aligned; there is no solid explanation for these jumps. The average displacement between the scans is again on the order of 0.3 micrometers.
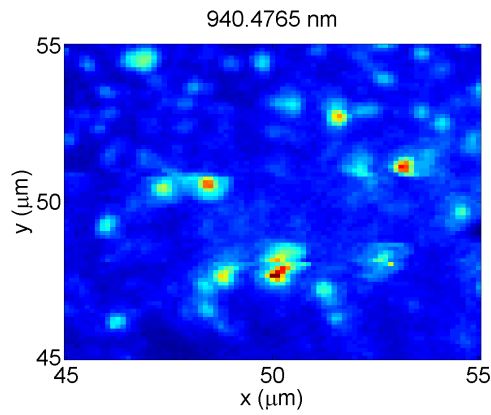
940.4765 nm

Figure 3.22: The jump in spatial scan are clearly visible. Multiple jumps can be seen in this image; it is unsure what caused these jumps. The top and bottom half are not aligned.
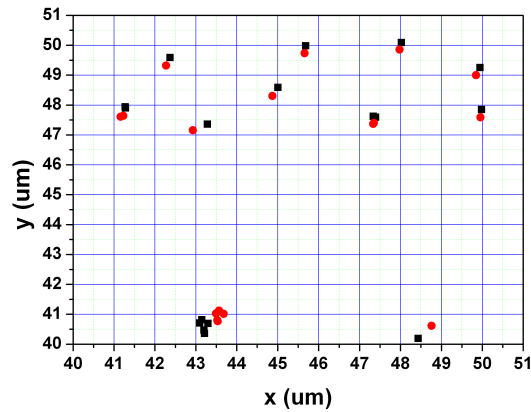

Figure 3.23: The repeatability of the positioning scans. The black and red spots represent the positions of the cross scans before and after the spatial scans respectively. There are no data points in the middle section because of the jump in the spatial scans. The average displacement is on the order of 0.3 micrometer, which should be accurate enough.

53

Chapter 4

Conclusion & Outlook

This thesis described the properties of microcavity quantum dot samples. A full procedure was given for getting a cavity degenerate by using the hole burning technique, in combination with other measurements such as voltage scans and spatial scans. Voltage tuning of the birefringence has been measured, and hole burning was observed to affect the emission of the quantum dots. It was found that the samples are degrading, but it is not yet sure what the cause of this degradation is. Obvious possibilities are the hole burning and the voltages and currents the sample has to endure.

Further suggestions on experiments that can still be carried out or repeated are for example

- From the bias voltage at which a dot is observed in the voltage scans, it is to some extent predictable whether the dot is in a neutral or a singly charged state. To verify the charged state exclusively, lifetime measurements can be performed. These are probably already being done by the time of finishing this thesis. The different charged states have different decay rates, which is observable using lifetime measurements. These measurements also provide a value for the Purcell enhancement. The Purcell enhancement can be obtained differently, as stated in [16], but first tries using this method failed.

- Concerning the setup itself, there is a possibility for expansion. A promising expansion would be the option for indpendent scanning. This means that it would be possible to independently position the imaging spot for photoluminescence, and the Tsunami spot for hole burning. In this way, the effect of hole burning on the cavity spectrum can be tracked in real time.

- To better understand the tendency for quantum dots to shift towards the higher wavelengths upon hole burning, a systematic study should be done. Although the effect has been observed multiple times by burning holes on the surface, the holes were never purposely burnt *inside* the trenches. Burning inside the trenches was

never necessary to obtain degenerate cavities, and is actually more dangerous than burning on the surface since it is closer to the active layer. Another study could be the dependence of this shifting on the burning power (and time).

- A more systematic study can be performed on the position of the holes to be burned. Although experience seems to be an important factor in getting cavities degenerate, a more detailed understanding would also help explain other effects such as the redshifting of the dots and the danger for degradation of the sample.

- Some cavities looked very promising, in the sense that they had a dot close to the FM center, and also tuned into the FM. Still, the reflection measurements did not show an all too surprisingly high peak, or sometimes even no peak at all. This might be due to dark states (if the dot was in the neutral charged state), or maybe even an effect of spin pumping.

- The measurements on the nonlinearity of the reflection peak could be repeated, with increased accuracy in the measuring of the power reaching the sample. Even though it is probably a coincidence the data showed two 'bumps' in the curve, the same behaviour was ironically also somewhat present in another paper [8].

- The voltage at which the dots emit was observed to shift as a function of power. Specifically, by increasing the power, the voltage dropped. This is most probably happening because higher pump power excites more carriers, and so at a lower voltage the probability for trapping excitons is already high enough.

- Another study can be done on the power needed for hole burning. Low powers did not seem to affect the degeneracy too much, but the quantum dots did respond. It is possible also that if a hole is burned with lower power, but on the same position, the sample gets damaged since the combined effect of two holes at the same position might be larger than one hole for a longer period.

Appendix A

Mode matching

Important note: These calculations were performed before a complete re-alignment was done. The insertion of the lens did not produce any visible change, indicating that the setup was actually mode-matched. This means that most likely an error has been made in the analysis.

In order to achieve maximum visibility of the reflection peak, the modes of the incoupling and outcoupling beams should be matched. Ideally, this means that the beams are exactly equal (in curvature and width) at every position. Using ray transfer matrices (ABCD matrices), beam properties can be calculated at any given point. The beams are described through a *q-parameter* [23], which is a complex valued parameter describing both the width w and curvature R of the beam as a function of distance (along the direction of travel, taken to be the z-axis)

$$\frac{1}{q(z)} = \frac{1}{R(z)} + i\frac{\lambda}{\pi w(z)^2}$$

If the q-parameters of the incoupling and outcoupling beams are known, the ABCD matrices can be used to find a configuration for one or multiple lenses which match the two beams. Figure A.1 shows a simplified sketch of the situation, and indicates the incoupling and outcoupling beams. The numbers shown in the image refer to positions at which CCD images were made, which will be discussed below.

Beam waist

To find the q-parameters of the beams, both the curvature and the width have to be known. In the following it is assumed that the beams are plane waves at the focus, so that at that specific position we can neglect the $1/R(z)$ term. To find the waists of the beams as a function of z, several images of the beam were taken using the CCD camera (Figure A.2 shows images of the outcoupling beam). By position the camera at different distances along the beam, information about the waist and its divergence can
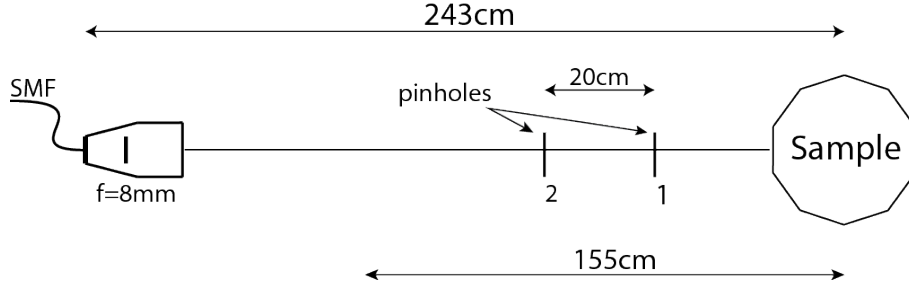
Figure A.1: Schematic of the mode-match situation. The incoupling beam goes from fiber to the sample, and the outcoupling beam goes from sample to fiber. The 243cm distance indicated includes the path travelled into the cryostat to reach the sample.

be extracted by fitting a Gaussian profile through the image. Both the incoupling beam (laser) and the outcoupled beam (the fundamental mode of the cavity) have a Gaussian profile. The waist w of a Gaussian beam along its propagation direction z is given by

$$w(z) = w_0 \sqrt{1 + \left(\frac{\lambda z}{\pi w_0}\right)^2} \tag{A.1}$$

where w_0 is the waist at the focus (taken to be at $z = 0$). Far away from the focus (i.e. for large values of z), the divergence of the beam is characterized by its divergence angle θ. From this divergence angle, the waist of the beam at the focus can be obtained through

$$w_0 = \frac{\lambda}{\pi \theta} \tag{A.2}$$

If the distances at which the CCD images were taken are indeed in this limit, then by rewriting equation A.1 to

$$z = \frac{\pi w_0^2}{\lambda} \sqrt{\frac{w^2}{w_0^2} - 1} \tag{A.3}$$

and substituting the values should provide a numerical check.

The two images shown in Figure A.2 have waists of 1.04mm and 1.21mm respectively, and were taken about 20cm apart. Hence the divergence angle θ is

$$\theta = \arctan\left(\frac{1.21mm - 1.04mm}{200mm}\right) \approx 0.05 \text{ degrees}$$

The emission from the dots is centered (on average) around 930nm, and so by using equation A.2 and the value for θ:

$$w_0 = \frac{930\text{nm}}{\pi \cdot 0.05} \approx 0.35\text{mm}$$

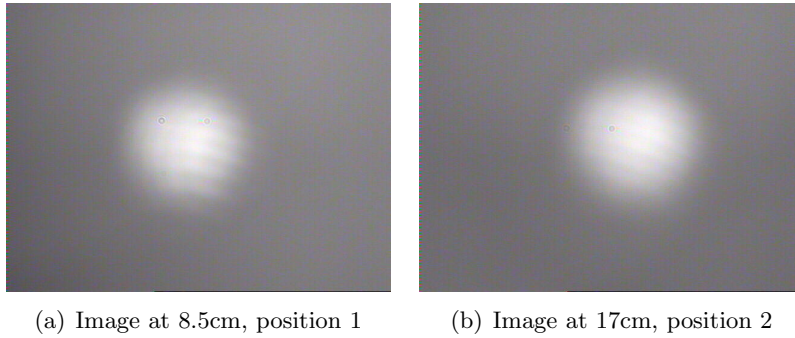(a) Image at 8.5cm, position 1   (b) Image at 17cm, position 2

Figure A.2: Images of the outcoupling beam, taken using the CCD camera. By fitting a Gaussian profile these images the waist of the beams can be extracted. The CCD images have pixels representing $7.5 \times 7.5\mu m$ areas. The waists of the beams are found to be 1.04mm for (a) and 1.21mm for (b).

To validate that we are indeed in the range which can be considered 'far from focus', subsitution of this result in equation A.3 results in the distances to the focus as seen from the two positions at which the images were taken

$$z_1 = 1.1745\text{m and } z_2 = 1.3752\text{m}$$

The distance between these two points is about 20.1cm, showing that we are indeed correct in the assumption. Repeating the same procedure for the incoupling side, we find a waist w_0 of 0.22mm, and a separation of 20.2cm.

Since the q-parameters for the outcoupling beam is now known, its waist at the position of the fiber can be determined. The length of the optical path from sample to fiber was measured to be 243cm, and the lens used to couple into the fiber has an 8mm focal length. Using ABCD matrices (consisting of a free space propagation part and a lens), the beamwaist at the fiber entrance is found to be $6.7\mu m$. The single mode fiber has a core diameter of $5\mu m$, meaning that we are roughly losing one order of magnitude (since $(2 \cdot 6.7/5)^2 \approx 16\%$) in light intensity.

By inserting one or multiple lenses, the beam waist can be corrected to match the fiber diameter. A first try has been given on mode matching using a single lens. Since we are limited by the space on the optical table, the easiest way to do the mode matching is by calculating the required focal length of the lens for a given position. This can be done again using ABCD matrices. A 60cm focal length at at distance of 1.55m from the sample was calculated to be necessary; the fine-tuning of the exact position can then be done empirically. Little or no effect was seen by inserting the lens.

Appendix B

Additional file listing

This appendix lists the most important assets/files used in analyzing and obtaining data. Folders and subfolders for the locations of these files have not been included.

B.1   Matlab scripts

The following Matlab scrips were written and used:

- `QDStarkShift.m` for reading and processing the voltage scans.

- `Fit2D.m` for fitting intensity profiles through 2D images for distance extraction.

- `FitPeak.m` for fitting and processing the reflection scans.

- `Matrix3DPlot.m` for processing the spatial scan data

- `Cross_Scan_Positioning.m` for fitting the marker dips.

- `Polarization_Separation.m` for fitting two reflection dips and extracting their separation.

- `HermitePolynomial.m` for numerical evaluation of the first three Hermite polynomial functions.

- `CavityModes.m` for plotting the first few cavity modes.

- `FMW.m` for calculating the fundamental mode waist.

B.2   Python

Python was extensively used for writing measurement programs. A few of the most used files are listed here.

- `SpatialScan.py` for performing spatial scans.

- `StarkShiftScan.py` for doing a voltage scan.

- `RealTimeAlignment.py` for real-time reflection spectroscopy.

- `LaserScan.py` for scanning the reflection as a function of voltage.

- `positioningScan.py` like the spatial scan file, but used for the positioning scans.

- `APDScan.py` was used for scanning the reflection with the APDs.

B.3 Maple files

Some Maple 13 files were used to do calculations on the mode matching

- `RayTracing.mw`

- `BeamWaist.mw`

- `ModeMatchSingleLens.mw`

- `ModeMatchTwoLenses.mw`

B.4 Origin

Origin was also extensively used to gather all data in separate tables, and to do easy fits (more complicated or extensive fits were done using Matlab scripts). Some of the most important Origin projects are listed here.

- `DotShifting.opj` for tracking the spectral shifting of the dots by hole burning.

- `Power.opj` for the nonlinearity measurements.

- `Movement_of_Positioning_Scan.opj` to quantify the positioning scan stability.

- `PolScan.opj` for analyzing the polarization scans.

- `VoltageBirefringence.opj` was made to quantify the voltage birefringence.

B.5 Summaries

During the project several short summaries were written. Some of them have been rewritten and used in this thesis, while some others provide the full data of which only part (or just the conclusion) were taken into account in this document.

- `Positioning.pdf` contains the calculated positions and voltage scans for the selected dots on the positiong sample.

- `R2C5.pdf` complete summary of R2C5 cavity, including degeneracy procedure.

- `FMW.pdf` summarizes the fundamental mode waist data.

- `Summary.odt` was the first summary, containing data on the intensity and dot distance.

- `StarkEffectSummary.odt` about the first few voltage scans.

References

[1] G. Burkard D.P. DiVincenzo D. Loss M. Sherwin A. Imamoglu, D. D. Awschalom and A. Small. Quantum information processing using quantum dot spins and cavity qed. *Phys. Rev. Lett.*, 83(20):4204–4207, Nov 1999.

[2] Alexia Auffèves-Garnier, Christoph Simon, Jean-Michel Gérard, and Jean-Philippe Poizat. Giant optical nonlinearity induced by a single two-level system interacting with a cavity in the purcell regime. *Phys. Rev. A*, 75(5):053823, 2007.

[3] R. Blatt and D. Wineland. Entangled states of trapped atomic ions. *Nature*, 2008.

[4] Cristian Bonato, Florian Haupt, Sumant S. R. Oemrawsingh, Jan Gudat, Dapeng Ding, Martin P. van Exter, and Dirk Bouwmeester. Cnot and bell-state analysis in the weak-coupling cavity qed regime. *Phys. Rev. Lett.*, 104(16):160503, Apr 2010.

[5] J. Gudat S. Thon H. Kim P. M. Petroff M. P. van Exter C. Bonato, D. Ding and D. Bouwmeester. Tuning micropillar cavity birefringence by laser induced surface defects. *Appl. Phys. Lett.*, 95:255104, 2009.

[6] M. A. Cusack, P. R. Briddon, and M. Jaros. Electronic structure of inas/gaas self-assembled quantum dots. *Phys. Rev. B*, 54(4):R2300–R2303, Jul 1996.

[7] I. Fushman N. Stoltz P. Petroff D. Englund, A. Faraon and J. Vuckovic. Controlling cavity reflectivity with a single quantum dot. *Nature*, 450:857–861, 2007.

[8] I. Fushman N. Stoltz P. Petroff D. Englund, A. Faraon and J. Vuckovic. Controlling cavity reflectivity with a single quantum dot. *Nature*, 450:06234, 2007.

[9] C.R. Monroe D. Kielpinski and D.J. Wineland. Architecture for a large-scale ion-trap quantum computer. *Nature*, 417:709–711, 2002.

[10] K. de Vries. Optical modes of micropillar cavities, August 2009.

[11] M. Fox. *Quantum Optics - An Introduction*. Oxford University Press, 2006.

[12] E.T. Jaynes and F.W. Cummings. Comparison of quantum and semiclassical radiation theories with application to the beam maser. *Proc. IEEE*, 51(1):89–109, 1963.

[13] P. Frigeri P. Allegri V. Avanzini L. Seravalli, M. Minelli and S. Franchi. The effect os strain on tuning of light emission of energy of inas/ingaas quantum-dot nanostructures. *Appl. Phys. Lett.*, 82:2341, 2003.

[14] Chuang M. Nielsen and L. Isaac. *Quantum Computation and Quantum Information*. Cambridge Univserity Press, 2000.

[15] P. Michler. *Single Semiconductor Quantum Dots*. Springer, 2009.

[16] M. Munsch, A. Mosset, A. Auffèves, S. Seidelin, J. P. Poizat, J.-M. Gérard, A. Lemaître, I. Sagnes, and P. Senellart. Continuous-wave versus time-resolved measurements of purcell factors for quantum dots in semiconductor microcavities. *Phys. Rev. B*, 80(11):115312, Sep 2009.

[17] W. Tittel N. Gisin, G. Ribordy and H. Zbinden. Quantum cryptography. *Rev. Mod. Phys.*, 74:145–195, 2002.

[18] S. Strauf A. Badolato D.D. Lofgreen P.M. Petroff L.A. Coldren N.G. Stoltz, M. Rakher and D. Bouwmeester. High-quality factor optical microcavities using oxide apertured micropillars. *Appl. Phys. Lett.*, 87(3):031105, 2005.

[19] G. L. W. Hart P.R.C. Kent and A. Zunger. Biaxial strain-modified valence and conduction band offsets of zinc-blende gan, gap, gaas, inn, inp, and inas, and optical bowing of strained epitaxial ingan alloys. *Appl. Phys. Lett.*, 81:4377, 2002.

[20] E.M. Purcell. Resonance absorption by nuclear magnetic moments in a solid. *Phys. Rev. Lett.*, 69:37–38, 1946.

[21] M. T. Rakher, N. G. Stoltz, L. A. Coldren, P. M. Petroff, and D. Bouwmeester. Externally mode-matched cavity quantum electrodynamics with charge-tunable quantum dots. *Phys. Rev. Lett.*, 102(9):097403, Mar 2009.

[22] Matthew T. Rakher. *Quantum Optics with Quantum Dots in Microcavities*. PhD thesis, University of California, Santa Barbara, December 2008.

[23] B. Saleh and M. Teich. *Fundamentals of Photonics*. Wiley-Interscience, 1991.

[24] C. Santori. *Generation of nonclassical light using semiconductor quantum dots*. PhD thesis, Stanford University, April 2003.

[25] J. T. Shen and Shanhui Fan. Coherent photon transport from spontaneous emission in one-dimensional waveguides. *Opt. Lett.*, 30(15):2001–2003, 2005.

[26] Susanna M. Thon, William T. M. Irvine, Dustin Kleckner, and Dirk Bouwmeester. Polychromatic photonic quasicrystal cavities. *Phys. Rev. Lett.*, 104(24):243901, Jun 2010.

[27] Edo Waks and Jelena Vuckovic. Dipole induced transparency in drop-filter cavity-waveguide systems. *Phys. Rev. Lett.*, 96(15):153601, 2006.

[28] P. Yu and M. Cardona. *Fundamentals of Semiconductors*. Springer, 2001.